ChemComm

FEATURE ARTICLE

View Article Online
View Journal | View Issue

Cite this: *Chem. Commun.*, 2025, **61**, 11131

Structure–property relationships of Group IV (Si–Ge–Sn) semiconductor nanocrystals and nanosheets – current understanding and status

Jeremy B. Essner, † Maharram Jabrayilov, † Andrew D. Tan, Abhishek S. Chaudhari, Abhijit Bera, Brodrick J. Sevart and Matthew G. Panthani *

Received 3rd October 2024,
Accepted 8th May 2025

DOI: 10.1039/d4cc05199h

rsc.li/chemcomm

Group IV semiconductor nanomaterials, including silicon nanocrystals and more recently nanosheets, are emerging as promising candidates for next-generation optoelectronic applications due to their tunable room-temperature photoluminescence and compatibility with CMOS technologies. However, the intrinsic indirect bandgaps of Group IV seminconductors remains a key limitation. Here, we highlight our group's contributions toward understanding structure–property relationships in solution-processable Group IV semiconductor nanocrystals and nanosheets - specifically, understanding how their structure, surface chemistry, and chemical composition influence affect properties such as bandgap.

1 Introduction

Nanostructured Group IV semiconductors comprised of Group IVA (or Group 14) elements have emerged as promising materials for next-generation optoelectronic devices.[1–4] Group IV semiconductors are relatively abundant, inexpensive, and non-toxic; they also offer a key advantage over other prospective materials such as IIIA–VA (*e.g.*, GaAs, GaN, InAs) and (metal halide) perovskites in that they are compatible with the CMOS process, enabling seamless integration into the existing microelectronic infrastructure.[5,6] Table 1 summarizes the key advantages of Group IV semiconductors over other semiconductor classes. The primary challenge in using conventional Group IV semiconductors for many applications is their indirect bandgaps,[7] which make them poor light emitters, even at cryogenic temperatures.[8] This fundamental challenge can potentially be overcome by confining the physical dimensions of these materials to the nanoscale in one, two, or three dimensions to create 2D nanosheets (NSs), 1D nanowires, 0D nanocrystals (NCs). Indeed, nanostructuring has been shown to dramatically enhance photoluminescence (PL) in Group IV nanostructures.[9–11] Another approach to improving light emission has been the synthesis of Group IV nanoalloys (*e.g.*, $Si_{1-x}Ge_x$, $Ge_{1-x}Sn_x$, $Si_{1-x}Sn_x$, or $Si_{1-x-y}Ge_xSn_y$),[12–18] in which the random distribution of the Group IV elements within the alloy may break the translational symmetry that gives rise to the indirect bandgaps of bulk Si and Ge.[19]

Many prior efforts have targeted the issue of band structure in Group IV semiconductor nanomaterials; however – with the exception of Si-based nanomaterials – they are often characterized by relatively weak or non-existent light emission (Φ_{PL} often below 10%) due to (i) poorly understood synthesis–structure relationships, (ii) loosely established, and sometimes conflicting, structure–property relationships, including the role that surface states/chemistry play, and (iii) elusive origins of light emission in as-prepared materials. Thus, deeper understanding of these nanomaterials' structure, chemistry, and properties is necessary to achieve commercial viability.

Here, we highlight our contributions to the broader understanding of structure–property relationships in Group IV semiconductor nanomaterials, with a particular focus on SiNCs and SiNSs. Specifically, we summarize how synthetic conditions, structure, morphology, surface chemistry, and composition influence the optoelectronic properties, namely the band structure and PL (Scheme 1). Lastly, we conclude with broad challenges for these materials and suggest potential paths forward.

2 Nanocrystals

Group IV semiconductor NCs have been investigated for many decades due to their potential use in solar cells,[20] light emitting diodes,[11] and photodetectors.[21] The interest in the field began in the early 1990s with the synthesis of 3 nm silicon crystallites *via* electrochemical etching of silicon wafers, resulting in red emission,[22] followed by the synthesis of highly luminescent (Φ_{PL} of 5–20%) hydride- and alkoxide-terminated SiNCs in the

Iowa State University, 618 Bissell Road, 2037 Sweeney Hall, Ames, Iowa 50011, USA. E-mail: panthani@iastate.edu; Tel: +1-515-294-1736

† These authors contributed equally to this work.

Table 1 Key advantages of Group IV semiconductors based on Group IVA elements compared to other classes of state-of-the-art semiconducting materials based on IIIA–VA and IIB–VIA elements. Note, the abbreviations MIR and NIR mean mid-infrared and near-infrared, respectively

Property	Group IV	Group III–V/II–VI
CMOS compatibility	Excellent	Requires heterointegration
Commercial viability	High (low cost, abundant)	Low (high cost, scarce)
PL quantum yield (Φ_{PL})	Improved with nanostructuring and alloying	Requires complex production for high values
Band structure engineering	Alloying or strain affords visible to MIR tunabilty	Requires elaborate heterostructures; restricted to NIR
Environmental impact	Minimal to none (nontoxic, sustainable)	High (toxic)

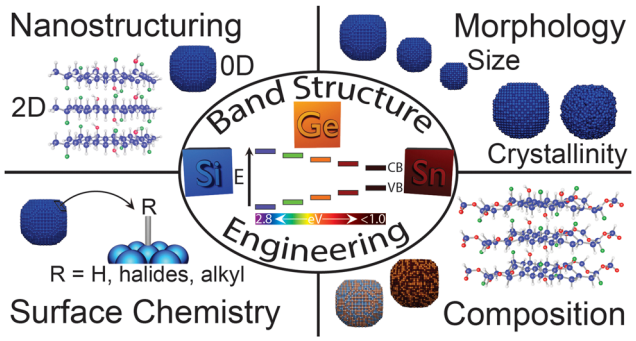

Scheme 1 Factors influencing electronic properties in solution-processable Group IV semiconductor nanomaterials towards band structure engineering.

2000s;[23] these NCs also displayed electrogenerated chemiluminescence.[24] From 2005 to present, our group has made notable contributions to understanding structure–property relationships of Group IV NCs, as outlined below.

2.1 Silicon nanocrystals

2.1.1 Synthesis. In earlier work on SiNC synthesis, we demonstrated the colloidal synthesis of SiNCs from high-temperature pyrolysis (1100 to 1400 °C) of hydrogen silsesquioxane (HSQ),[25–27] as HSQ had recently been demonstrated as a promising precursor at the time.[28] While HSQ has historically been the primary precursor employed for generation of SiNCs since,[4] synthetic challenges and short shelf life have led to high costs and restricted commercial availability. Thus, to overcome these challenges, our group and others more recently demonstrated that SiNCs could be generated from silicon monoxide (SiO) at lower pyrolysis temperatures (900 to 1100 °C).[29,30] Our group is also exploring HSQ-like, sol–gel polymers ($(RSiO_{3/2})_n$ where R = H, alkyl, or aryl), derived from halo- or organosilanes, as precursors for SiNCs, as such "HSQ polymers" have recently been demonstrated as a promising alternative to HSQ.[31]

2.1.2 Structure. High temperature processing of the Si precursor (900 to 1400 °C) leads to nanoscale Si domains, consisting of tetrahedrally coordinated Si atoms in a diamond cubic lattice, embedded within a SiO_2 matrix, which are then liberated from the SiO_2 matrix *via* hydrofluoric (HF) acid etching (see Surface chemistry section),[25–27,29] with the duration of this latter step also impacting the resultant nanocrystal size.[32] Our early work on SiNCs demonstrated that higher processing temperatures of HSQ (900 to 1400 °C) yield larger crystalline domains (approximately 3 nm to 90 nm) due to increased malleability or melting of the HSQ precursor (Fig. 1);[25] others have recently reported similar results.[33] Additionally, we studied the structure of the HSQ-derived SiNCs *via* high-resolution transmission and scanning transmission electron microscopies (TEM and STEM) using graphene as an ultrathin support, which afforded microscopic imaging of defects (twinned planes) and lattice strain in the nanocrystals (Fig. 2).[26] Since, others have employed this imaging approach to elucidate more detailed structural information of SiNCs derived from SiO.[30] Such high-resolution microscopic imaging of the NCs' intricate structure is vital to improving understanding of the NCs' structure–property relationships, especially since Thiessen *et al.* more recently demonstrated *via* ^{29}Si solid-state nuclear magnetic resonance spectroscopy that SiNCs derived from HSQ form three structural layers: a crystalline core, a quasi-crystalline subsurface, and a disordered surface.[34] The thermal processing of sol–gel polymers also results in temperature-dependent NC size.[35] In our recent work utilizing SiO as the SiNC precursor, we employed a single processing temperature (910 °C),[29] as this approach currently does not afford the same degree of temperature-dependent size tunability (approximately 2 nm to 5 nm).[30]

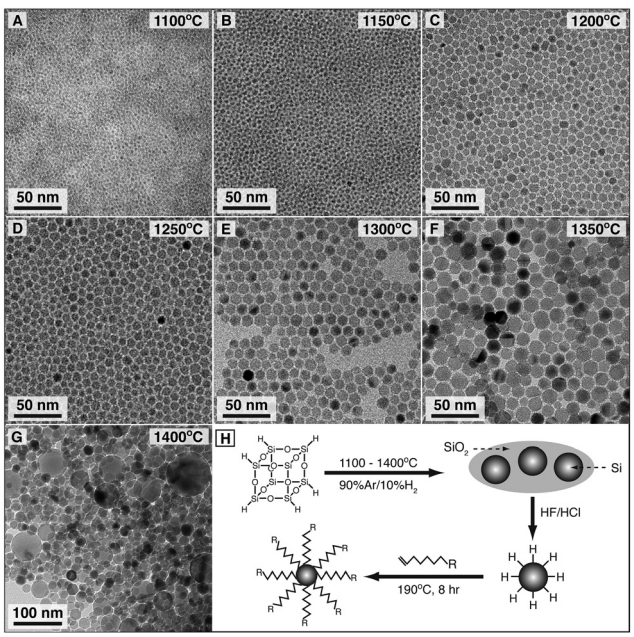

Fig. 1 (a)–(g) TEM of alkyl-terminated SiNCs generated through HSQ decomposition at the indicated temperatures, followed by HF etching and thermal hydrosilylation with terminal alkenes, as schematically shown in panel (h). (Reproduced with permission from ref. 25 Copyright 2012 American Chemical Society).

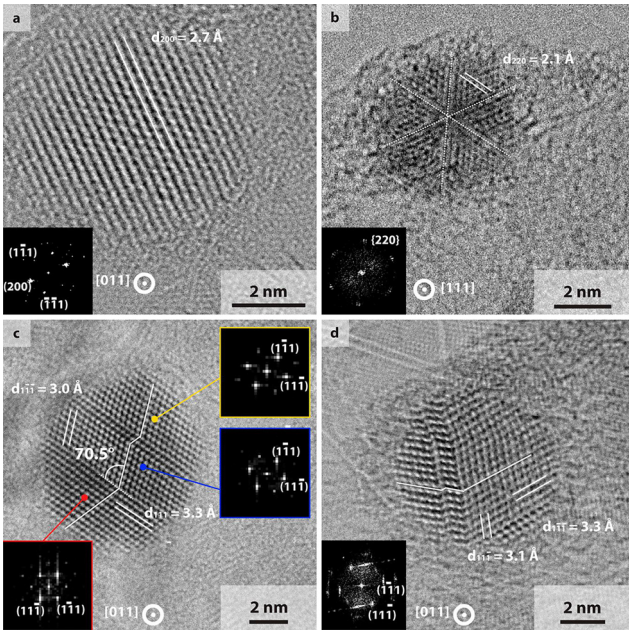

Fig. 2 The defect free (a) and twinned lattice structure (b)–(d) of SiNCs acquired with bright-field STEM. The alkyl-passivated SiNCs were demonstrated in panels (a), (c) and (d) whereas hydride-terminated silicon nanocrystal was shown in panel (b) (Reprinted with permission from ref. 26 Copyright 2012 American Chemical Society).

2.1.3 Surface chemistry. The surface chemistry of the as-synthesized SiNCs is highly dependent upon the synthetic protocol employed with both hydrogen and halide surface groups reported.[36,37] Our works demonstrated that the surface of SiNCs, derived from thermally processed HSQ and liberated with HF etching, is primarily terminated by SiH_x groups,[25–27,29] with others reporting that the NCs' surface consists roughly of 54 to 62% mono- (–SiH), 25 to 38% di- ($–SiH_2$), and 8 to 20% trihydride ($–SiH_3$) groups.[38] We note, when HF etching is employed, minor fluorine termination ($\leq$0.5 fluorine nm^{-2}) is also reported to arise.[36] Unfortunately, the reactive SiH_x groups lead to poor chemical stability, with exposure to oxygen or water resulting in an insulating oxide layer.[39] To overcome this chemical instability, we employed a hydrosilylation approach,[25–27,29] in which the Si–H groups are reacted with terminal alkenes (or alkynes), such as 1-dodecene (1-DD) or 1-octadecence (1-OD),[25,26] to form Si–C bonds and an alkyl-terminated surface. These hydrosilylation surface termination reactions proceed due to the formation of silyl radicals, which are typically generated thermally,[25–27,29] by light,[40] or by chemical initiators.[41] While most literature reports passivate SiNCs with a single alkene of a given chain length, we found that the combination of long and short alkenes (4 : 1 ratio 1-DD : 1-OD) enhanced the ligand surface coverage and colloidal stability of SiNCs, especially for NCs greater than approximately 8 nm.[25] Additionally, rigorous purification of the passivated NCs is key for removing impurities, such as residual ligand, that can interfere with (optical) characterization. Towards this, we found that multiple solvent/antisolvent washing/precipitation cycles were highly effective for removing impurities and obtaining clean, optically

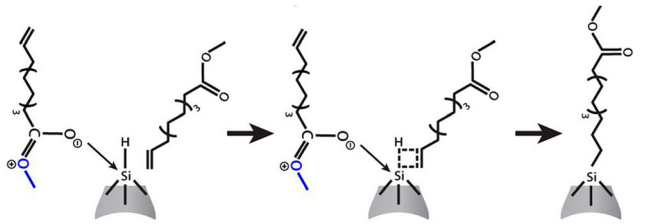

Fig. 3 Mechanistic illustration of room temperature hydrosylilation of silicon nanocrystals in the presence of methyl 10-undecenoate. The methyl 10-undecenoate was demonstrated in its resonance structure to highlight electrostatic interaction with the hydride-terminated silicon nanocrystal surface. (Reproduced with permission from ref. 27 Copyright 2013 American Chemical Society).

transparent SiNC dispersions.[25] Further, we also demonstrated that hydrosilylation of SiNC surfaces can be facilitated by either ω-ester-terminated (alkene-COOR) or ω-acid-terminated alkenes (alkene-COOH) at room temperature,[27] where the bifunctional ligands catalyze the hydrosilylation process by the nucleophilic carbonyl group of the ester (or acid) enhancing coordination with the oxophilic silicon surface and thereby the reactivity of silicon–hydrogen (Si–H) species toward the terminal alkenes, as shown in Fig. 3.

2.1.4 Structure–property relationships. Hydride-terminated SiNCs are known to display weak PL, while terminating the surface with alkyl groups markedly increases Φ_{PL},[42] consistent with predictions that alkyl termination improves radiative transitions.[43] We demonstrated that HSQ-derived SiNCs terminated with both 1-DD and 1-OD display Φ_{PL} values up to 8%, with the PL maxima redshifting and Φ_{PL} decreasing with increasing NC size (Fig. 4(a)). Others have also observed similar size-dependent optical properties for alkyl-terminated SiNCs, derived from HSQ or sol–gel polymers, with Φ_{PL} values up to 70% more recently reported; in addition to size, the observed optical properties are also dependent upon the precursor and ligand.[31,44] Conversely, Korgel and co-workers revealed that the Φ_{PL} of SiNCs larger 4.5 nm is not inherently dependent on their size,[45] while SiNCs smaller than 4.5 nm have size-dependent Φ_{PL} that decreased markedly with smaller NC size due to increased nonradiative relaxation.[45] Similarly,

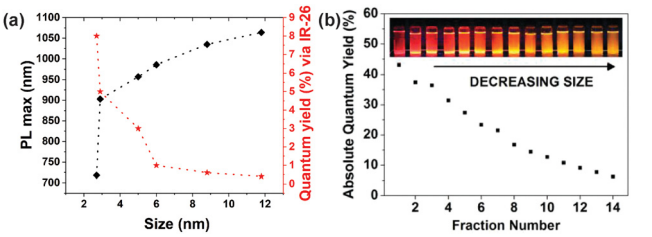

Fig. 4 The size-dependent photoluminescent properties of SiNCs. (a) The relationship between PL peak maximum and relative Φ_{PL} as a function of SiNC size. The Φ_{PL} values were assessed *vs.* the infrared-emitting, reference fluorophore IR-26. (b) Size-dependent absolute Φ_{PL} values of SiNCs obtained *via* size-selective precipitation. (Panels (a) and (b) were adapted with permission from ref. 25,46, respectively. Copyright 2012 American Chemical Society).

Ozin and colleagues reported a monotonic, size-dependent decrease in Φ_{PL} for SiNCs derived from SiO, terminated with allylbenzene, and fractionated *via* size-selective precipitation (Fig. 4(b)).[46] Table 2 summarizes the reported properties (size, PL peak maxima, Φ_{PL}) for alkyl-terminated SiNCs derived from HSQ, SiO, or HSQ polymers from select works, demonstrating that the properties of SiNCs are highly dependent on the precursor, passivating ligand, and NC size. While the size, crystallinty, and surface chemistry of the SiNCs are known to be key contributors to the observed PL,[4,47] the exact origin (*e.g.*, physical, chemical) of this PL remains elusive.

Another viable avenue for tuning the electronic properties of SiNCs is through alloying with germanium to yield $Si_{1-x}Ge_x$ NCs. Although our group has yet to publish work in this area, such alloys are predicted to have size-, shape-, and composition-dependent electronic properties[13,55] and can be synthesized and surface terminated *via* similar routes to SiNCs,[56–62] with size and compositional tunability arising from varied Si : Ge ratios[59] and reaction temperatures.[58,59] The as-synthesized hydrogen-terminated $Si_{1-x}Ge_x$ NCs are reported to have a PL peak maximum around 1.55 eV, with air oxidation blueshifting the PL energy about 0.1 eV due to a decrease in size,[56,57] while both blue PL (3.45 eV) and infrared PL (1.3 eV to 1.6 eV) have been observed, depending on the hydrosilylation reaction or ligand.[56,58,60–62]

2.2 Germanium nanocrystals

2.2.1 Synthesis. While numerous synthetic protocols have been reported for the preparation of GeNCs,[63] the majority of these synthetic routes require high-purity Ge precursors and toxic, flammable reducing agents to control the morphology of the GeNCs,[64,65] which are reported to produce unwanted byproducts and highly polydisperse NCs with dangling bonds, leading to poor optical properties.[66] To address these challenges, we synthesized GeNCs through thermal disproportionation of a germania (GeO_x) glass (250 to 425 °C); we prepared the germania glass *via* water hydrolysis of a $GeCl_2$·dioxane complex at room temperature (Fig. 5(a)).[67] Our approach afforded the growth of nanocrystalline germanium domains embedded in a GeO_2 matrix at lower annealing temperatures than previous reports using germanium oxides.[68–70]

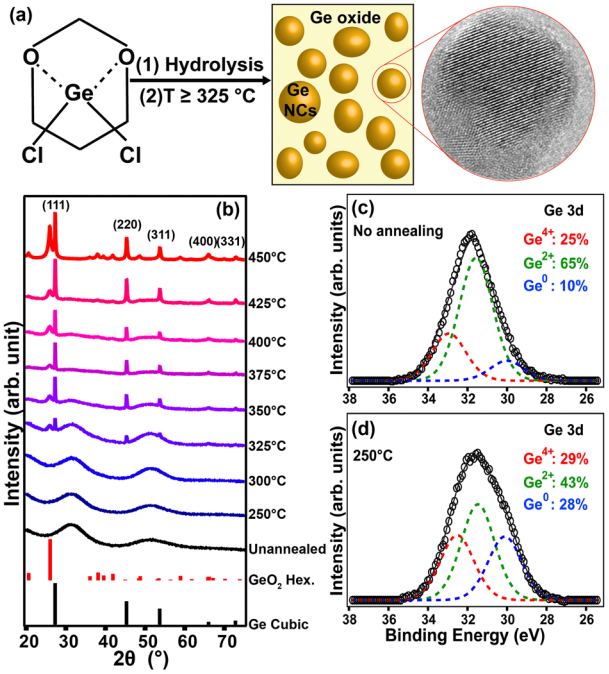

Fig. 5 (a) Schematic illustration of GeNCs synthesis *via* the thermally-induced disproportionation of hydrolyzed $GeCl_2$·dioxane. (b) XRD patterns of hydrolyzed $GeCl_2$·dioxane processed at different temperatures under N_2 flow. XPS of (c) unannealed and (d) annealed (250 °C) hydrolyzed $GeCl_2$·dioxane precursor indicating the formation of nanocrystals and amorphous GeO_2. (Reproduced from ref. 67 with permission from the Royal Society of Chemistry).

2.2.2 Structure. Typically, the crystallinity and size (2 to 30 nm) of GeNCs can be controlled by varying synthetic conditions such as the employed Ge precursor(s), annealing time and temperature, reducing agent, or ligand.[64–66,71–76] We employed *ex situ* X-ray diffraction, coupled with X-ray photoelectron spectroscopy, to observe the temperature-dependent formation of nanocrystalline domains in a GeO_2 matrix derived from GeO_x glass (Fig. 5(b)–(d)).[67] Our results indicated no significant

Table 2 Summary of SiNC size, peak PL, and Φ_{PL} for NCs synthesized from HSQ, SiO, or HSQ polymers and terminated with various alkyl groups. The ligand abbreviations, 1-P, 1-H, 1-O, 1-D, 1-DD, 1-DDY, 1-OD, 10-UDA, M-10-UD, and E-10-UD, represent the following terminal alkenes/alkynes used in the hydrosilylation step: 1-pentene, 1-hexene, 1-octene, 1-decene, 1-dodecene, 1-dodecyne, 1-octadecene, 10-undecenoic acid, methy-10-undecenoate, and ethyl-10-undecenoate, respectively

Precursor	Ligand	Size (nm)	Peak PL (eV)	Φ_{PL} (%)	Ref.
HSQ	1-DD, 1-OD	1.0–12.0	1.1–1.7	0.4–8.0	25
	10-UDA, M-10-UD, E-10-UD	2.3	1.9	7.0	27
	1-H, 1-DD, M-10-UD	3.0–5.0	1.4–1.8	30–70	10
	1-P, 1-DD, 1-DDY, M-10-UD	3.0–8.2	1.8	62	48
	1-D	2.7–3.9	1.7	38	49
SiO	1-D	3.5–4.0	1.5	4.0–16	30
	1-DD	2.9	1.5	—	29
HSQ polymer	1-DD	3.0–6.7	1.3–1.7	—	50
	1-DD	3.9–6.4	1.3–1.5	19–41	51
	1-OD	4.9	3.0	2.5–21	52
	1-O, 1-D, 1-OD	2.1–3.6	1.5–1.7	44–56	35
	M-10-UD	4–5	1.5	20–40	53
	10-UDA	1.8	1.7	22	54

structural change up to 325 °C, after which peaks assigned to amorphous GeO_x disappeared and peaks assigned to crystalline Ge emerged. Further, our XPS measurements confirmed that the disproportionation reaction started after 250 °C, as evidenced by an increase in the Ge^0 and Ge^{4+} signal and a decrease in the Ge^{2+} signal. We did not observe a clear temperature-dependence on the size of Ge nanocrystalline domains, contrary to the above reports, as well as others exploring thermal disproportionation of germanium oxides.[68–70] For instance, the thermal disproportionation of GeO between 410 °C and 550 °C produced GeNCs with dimensions ranging from 5 to 30 nm.[68] Further, our study of the thermal disproportionation of a GeO_x glass produced highly polydisperse GeNCs.[67] More recently, doping (*i.e.*, Co) of the Ge core was demonstrated to improve particle size uniformity.[77]

2.2.3 Surface chemistry. The resulting surface chemistry of GeNCs is highly dependent upon the synthetic protocol employed.[63] For example, solution-phase reduction of germanium halides with hydride-containing reducing agents[73,78] or HF-etched, thermally processed germanium oxides[69] result in hydride-terminated GeNCs (H-GeNCs), while thermolysis of alkylgermanes in the presence of alcohol is reported to result in GeNCs with alkoxy termination.[65] Based off this knowledge, we employed aq. HF etching to liberate the nanocrystalline Ge domains from our Ge oxide matrix, which resulted in hydride-terminated GeNCs.[67] As such H-GeNCs are prone to oxidation,[73,78] we then terminated the surface in a similar manner to H-SiNCs, using a (thermal) hydrogermylation approach with terminal alkenes (*e.g.*, octadecene) to yield alkyl- (1-OD-) terminated GeNCs;[67] such thermally activated, radical-initiated, or catalyzed hydrogermylation reactions are known to yield alkyl-terminated GeNCs with improved colloidal and chemical stabilities.[67,69,73,78] Additionally, nonthermal plasma and solution-based syntheses are reported to result in the formation of chlorine-terminated GeNCs, which were then reacted with a Grignard reagent to yield alkyl-passivated GeNCs.[79] Furthermore, simultaneous NC formation and surface termination with organic ligands has been reported,[71,72,75,76,80,81] with the employed capping ligands playing a significant role in NC growth[76] and the exchange of alkylamine ligands for dodecanethiol leading to increased ligand coverage.[81]

2.2.4 Structure–property relationships. Computationally, hydrogen-terminated GeNCs are predicted to have size-dependent optical properties due to quantum confinement effects, with the bandgap decreasing from 4.1 eV to 1.4 eV when the NC size increases from 1.25 nm ($Ge_{45}H_{58}$) to 3.96 nm ($Ge_{1445}H_{534}$).[13] Conversely, terminating the surface with more electronegative atoms, such as NH_2, F, Cl, Br, or hydroxyl, is predicted to lower bandgap energies, with halide and hydroxyl termination exhibiting greater stability compared to other terminal groups.[82] We did not observe detectable visible or infrared PL from our 1-OD-terminated GeNCs (derived from thermal disproportionation of germania glass), which we attributed to surface defects or impurities (*e.g.*, excess ligand),[67] although their polydispersity may be playing a role. Our observation of GeNCs with no detectable PL is consistent with other reports using similar oxide-based solid-state syntheses;[69] however, our results are contrary to many reports on GeNCs. Indeed, experimentally observed PL for H- or alkyl-terminated GeNCs is reported to range from the visible (2.95 eV) to infrared (0.67 eV), with both NC size and surface chemistry influencing the observed optical properties and increasing size typically red-shifting the PL.[71–73,75,76,78,83] For instance, multiple groups reported allylamine-capped GeNCs, 4 to 5.5 nm in size, with PL ranging from 2.95 eV to 2.30 eV,[73,78] as well as Φ_{PL} of up to 20% at visible wavelengths.[84] Similarly, alkyl-terminated GeNCs with visible PL spanning 4.1 eV to 2.5 eV and Φ_{PL} of up to 37% have been reported.[85] Conversely, others have demonstrated infrared-emitting alkyl(-amime)-passivated GeNCs, with size-dependent (2 to 18 nm) PL ranging from 0.67 to 1.44 eV,[71,72,75,76,83] often with low Φ_{PL} values (0.02 to 0.08%),[72,76] although, Φ_{PL} values of up to 8% have been reported.[71]

Similar to alloyed $Si_{1-x}Ge_x$ NCs, alloying of tin with germanium is a viable route for electronic property modulation. Again, while our group has yet to contribute to this area, $Ge_{1-x}Sn_x$ NCs alloys are predicted to have an indirect-to-direct bandgap transition with increasing Sn content,[12] with the simulated electronic properties of tetrahedrally coordinated NC alloys being dependent upon size, shape, and composition.[12,86,87] In general, $Ge_{1-x}Sn_x$ alloyed NCs are typically synthesized through convective or microwave heating of Ge and Sn halides (or Sn amides) in alkylamines, assisted by a (strong) reducing agent, such as *n*-butyllithium (*n*-BuLi), leading to alkylamine-terminated NCs, with the synthetic conditions impacting the size and composition.[88–91] Through these approaches, size- (1–20 nm) and composition- (up to 95% Sn) dependent electronic properties have been demonstrated, with increasing Sn content redshifting the absorbance onset and PL from the visible (2 eV) to the infrared (<1 eV),[86,87,89,91] while still maintaining the diamond cubic lattice.[90]

3 Two-dimensional nanosheets

In recent years, solution-processable methods, such as topotactic deintercalation of Zintl phase precursors (Fig. 6(a)),[92] have arisen as promising approaches towards free-standing Group IV NSs, as these approaches boast (i) less demanding and more cost-effective experimental conditions, (ii) higher synthetic throughput and yields, and (iii) improved chemical stability through, often *in situ*, surface termination (with hydrogen),[93] compared to bottom-up approaches such as epitaxial growth. Furthermore, this surface termination results in an opening of the bandgap,[9,94–97] with the Group IV NSs theoretically predicted to be (quasi-) direct bandgap semiconductors with excitonic optical absorption, sizeable bandgaps (silicane – 3.60 eV, germanane – 2.21 eV, and stanane – 1.35 eV), and strongly bound excitons, with binding energies of 0.40 to 1.07 eV, 0.33 to 0.92 eV, and 0.20 eV, respectively.[98,99] Additionally, the bandgaps of silicane and germanane have been computationally shown to be marginally affected by external electric fields, with a non-zero gap still existing at high field strength.[100] Furthermore, promising transport properties,[101,102] such as high carrier mobilities,[103,104] have

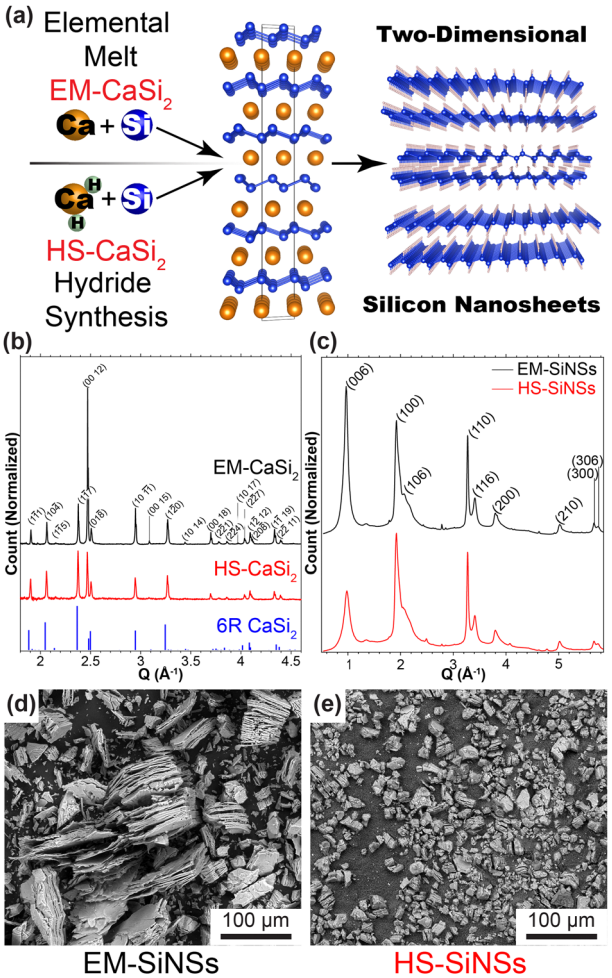

Fig. 6 Silicon nanosheets (SiNSs) synthesized by deintercalation of Ca^{2+} from calcium disilicide ($CaSi_2$); the $CaSi_2$ was prepared *via* both elemental melt (EM) and hydride synthesis (HS) approaches. (a) Schematic illustration of EM and HS approaches for the formation of Zintl phase $CaSi_2$ precursor. (b) Powder X-ray diffraction patterns of EM- and HS-$CaSi_2$. The 6R phase $CaSi_2$ reference pattern is shown in blue. (c) AI-spXRD of EM- and HS-SiNSs. SEM images of SiNSs derived from (d) EM and (e) HS approaches. (Modified with permission from ref. 111 Copyright 2023 American Chemical Society).

been demonstrated for silicane and germanane. These properties and potential electronic structure tunability make Group IV nanosheets enticing prospects for low energy, next-generation photonics, optoelectronics, or optical computing devices, with potential for integration into current silicon-based manufacturing infrastructure.[105] Indeed, Group IV NSs have recently shown promise in photosensitive devices.[106–110] The following sections highlight our contributions to structure–property relations in 2D Group IV nanosheets, with an emphasis on 2D Si and the overall focus on nanosheets derived from the topotactic deintercalation of Zintl phase compounds.

3.1 Silicon nanosheets

3.1.1 Synthesis. While various solution-processed synthetic protocols for free-standing two-dimensional silicon nanosheets (SiNSs) have been reported,[112–115] SiNSs are most frequently prepared through reaction of the layered Zintl phase precursor, calcium disilicide ($CaSi_2$), with (cold; <0 °C) aqueous (aq.) hydrochloric acid (HCl).[103,116–119] However, widely variable synthetic conditions, such as the source of $CaSi_2$ (commercial *vs.* laboratory scale), the concentration of hydrochloric acid (ranging from 1 to 12 M), and the deintercalation conditions, which encompass temperature (−35 °C to ambient, or higher) and time (ranging from hours to weeks), have been reported, leading to ambiguity regarding synthesis–structure relationships. We have published numerous works employing the following synthetic protocol, $CaSi_2$ decalciated by 12.1 M HCl at −35 °C for 10 to 14 days, that have led to increased understanding of the synthesis–structure relationships for SiNSs, as highlighted below.[9,96,97,111,120,121]

3.1.2 Structure. Numerous structures have been proposed for SiNSs derived from $CaSi_2$ since their first preparation over 150 years ago.[122–126] In historic structural models, the two-dimensional Si network present in the $CaSi_2$ precursor was assumed to be disrupted and reconstructed during the deintercalation step to yield layers consisting of mixed Si–Si and Si–O bonds,[127,128] however, latter works suggested that the preparation of SiNSs is a topotactic deintercalation.[123,125] We confirmed this supposition, demonstrating that, under experimental conditions commonly employed (−30 °C or lower, concentrated HCl, 10–14 days), the resulting material consists of stacks of individual Si monolayers in which the Si atoms are arranged in a buckled, six-membered honeycomb lattice, identical to the silicon layers in the $CaSi_2$ precursor.[9,96] Representative diffraction patterns and SEM are provided in Fig. 6(b)–(e). Further, our synchrotron-based total X-ray scattering results revealed that the stacking sequence of the monolayers closely resembles that of the initial stacking configuration observed in $CaSi_2$, albeit with a notable degree of anisotropic disorder; that is, disorder exists within the intersheet spacing but there is little turbostratic twisting or translational disorder among adjacent SiNSs.[96]

Precise control over the $CaSi_2$ polymorphism is expected to impact their properties.[129,130] Yao *et al.* very recently predicted that the stacking order of the $CaSi_2$ precursor should strongly influence the electronic properties of SiNSs. SiNSs derived from 1H and 6R polytypes are expected to exhibit interlayer charge transfer while those derived from the 3R polytype is not expected to exhibit interlayer charge transfer.[131] Further, it is important to have phase-pure Zintl phase precursors in order to properly draw conclusions regarding structure–property relationships.[9] While most commercial sources of $CaSi_2$ contain CaSi, Si, or $FeSi_2$ impurities, washing the precursor with a strong base is reported to remove bulk Si impurities;[116] however, $FeSi_2$ has proved difficult to remove.[132] Given these impurity issues, we investigated two different synthetic approaches for the preparation of high-purity 6R-$CaSi_2$, specifically, (i) the conventional elemental melt (EM) method and (ii) a less explored hydride synthesis (HS; Fig. 6).[111] The primary advantage of the latter is the reaction occurs at temperatures below the peritectic decomposition of $CaSi_2$. Although we produced high-purity $CaSi_2$ through both approaches, as confirmed by pXRD (Fig. 6(b)), the EM approach resulted in preferential, isotropic growth of $CaSi_2$ along the *c*-axis

while the HS method yielded more uniform $CaSi_2$ crystals with shorter lateral dimensions (see (00 12) reflection in Fig. 6(b)). We found that these features translated to the SiNSs upon deintercalation, with those resulting from the EM method having significantly larger lateral dimensions than the SiNSs resulting from the HS method (Fig. 6(d) and (e)). Our conclusion was further supported by azimuthally integrated synchrotron powder X-ray diffraction (AI-spXRD) measurements taken at Argonne National Lab (Fig. 6(c)), which displayed a more intense (006) reflection for the EM-SiNSs compared to the HS-SiNSs.

More recently, we demonstrated that the siloxane (Si–O–Si) content previously observed in SiNSs primarily originates from oxidation of silicon monolayers by dissolved oxygen in the deintercalant solution (*i.e.*, HCl), although, exposure to oxygen at any point after deintercalation will also contribute to (further) oxidation of the backbone, through oxygen insertion between Si–Si bonds.[121] Literature has demonstrated that these siloxanes (and other silicon oxides) can be removed through HF treatment,[117] however, this may be problematic depending on the desired application, as the etching of the inserted oxygen from the Si framework will effectively cleave the SiNSs, reducing their lateral dimensions. Furthermore, our results suggest that oxidation of the Si framework leads to further buckling of the monolayers which pushes the layers apart, evident by an increase in interlayer spacing with increasing oxygen exposure.[121]

Lastly, we investigated the structural impact on the SiNSs upon annealing for 10 min at temperatures between 100 and 400 °C (Fig. 7(a) and 8(b)).[96] Both our pair distribution function (PDF) and spXRD results indicated minimal degradation of the silicon monolayers up to 300 °C, after which, the monolayers showed increasing amorphization with higher annealing temperature; that is, the SiNSs began to crosslink *via* amorphous Si–Si bond formation resulting in a coalesced amorphous silicon structure, evidenced by the smoothing of PDF peaks and broadening of peaks in spXRD due to increased disorder as annealing temperature increased.

3.1.3 Surface chemistry. Conflicting conclusions exist in the literature about the exact surface chemistry for the as-prepared SiNSs generated *via* HCl deintercalation, with varying ratios of hydrogen to hydroxyl termination suggested.[9,97,122,125,133] Previously, we demonstrated that the surface composition of SiNSs, prepared from $CaSi_2$ deintercalated with concentrated HCl at −35 °C for 10–14 days, are mostly hydrogen terminated with possibly minor chlorine and hydroxyl termination.[9] More recently, we revealed, *via* solid-state nuclear magnetic resonance spectroscopy, that the surface composition of SiNSs prepared under these conditions consists of roughly 70% hydrogen, 20% chlorine, and 10% hydroxyl termination ($SiH_{0.7}Cl_{0.2}(OH)_{0.1}$).[97] Further, we demonstrated that these surface terminations are lost when the material is annealed (Fig. 7(c)) or oxidized (by O_2).[96,121] In the case of the former, we demonstrated that HCl gas is liberated as a byproduct,[9] while for the latter, the exact oxidative mechanisms and byproducts are still under investigation; however, our results suggest that oxygen is not inserted between Si–H bonds (forming Si–OH groups) but inserts into the silicon framework (*via* initial attack at SiH_3/SiH_2 sites) forming siloxanes.[121]

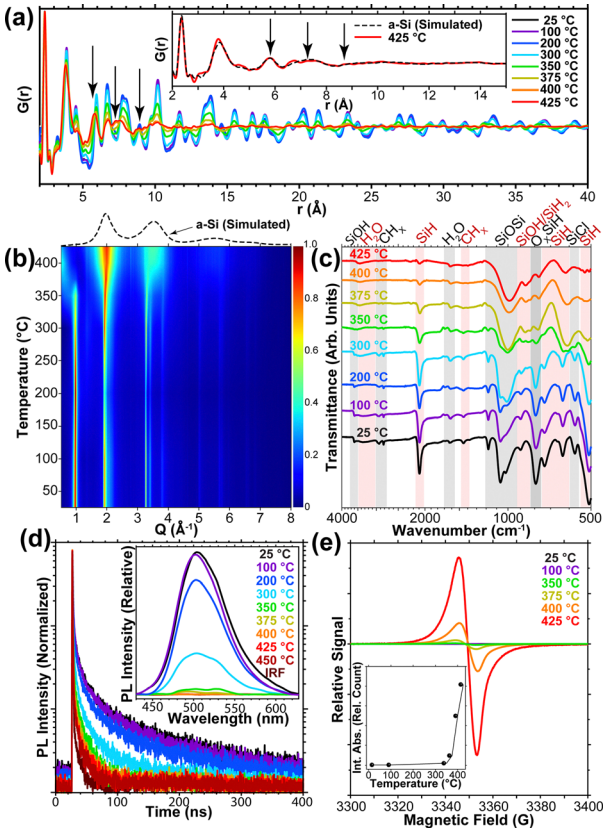

Fig. 7 Impact on the structure, chemistry, and optical properties of SiNSs upon annealing. (a) PDF of SiNSs annealed at various temperatures. Inset shows agreement of simulated and experimental results for SiNSs annealed at 425 °C. (b) AI-spXRD mapped over temperature showing amorphization starting around 300 °C. (c) FTIR of annealed SiNSs indicating loss of surface groups as annealing temperature increases. (d) Time-resolved and steady-state (inset) PL of annealed SiNSs. (e) EPR response of annealed SiNSs indicating generation of dangling bonds at higher annealing temperatures. Inset shows relative integrated EPR absorbance. (Reproduced with permission from ref. 96 Copyright 2021 American Chemical Society).

Literature also suggests that the quantity of hydroxyl groups on the SiNS surface can be increased *via* longer deintercalation time,[134] post-deintercalation water exposure,[135] or $CaSi_2$ deintercalation with $FeCl_3$ (along with trace water, followed by an HCl wash),[114] however, increasing siloxane content, evidenced by more intense Si–O–Si vibrations in FTIR, is frequently observed, suggesting that oxygen insertion into the Si framework is simultaneously occurring. These oxides are reportedly removed through HF treatment, leading to increased hydrogen termination, however, fluoride termination also arises.[117] Further, the formation of alkoxy termination through reactions between alcohols and Si–H_x (or Si–Cl groups) has been reported.[125,136]

As SiNSs are primarily hydrogen terminated when prepared with cold (mineral) acids,[9,96,97,111,121] the surface chemistry can be further altered through surface modifying, nucleophilic substitution or addition reactions widely reported for silicon surfaces,[95,137] such as hydrosilylation,[138–140] amination,[106] or Grignard strategies,[141] affording termination with various organic moieties tethered to the SiNSs *via* Si–C–R, Si–N–R, or Si–O–R linkages.

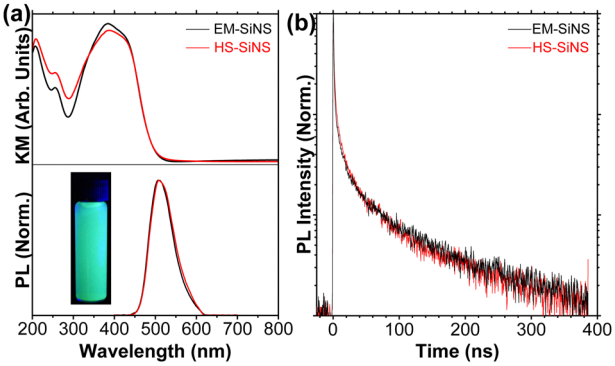

Fig. 8 Measurements of optical properties of EM and HS SiNSs. (a) Kubelka–Munk transformation of diffuse reflectance (top), used as a representative absorbance spectra of the SiNSs. Steady-state PL emission spectra of SiNSs excited at 370 nm (bottom). (b) Time-resolved PL of SiNSs excited at a wavelength of 359 nm and measured at 510 nm. (Modified with permissions from ref. 111 Copyright 2023 American Chemical Society).

Furthermore, simultaneous decalciation and organic termination has been reported.[142,143]

3.1.4 Structure–property relationships. Numerous computational studies have emerged in an effort to understand the impact that the structure and surface chemistry of SiNSs have on the materials' electronic properties. For instance, structural changes (*e.g.*, conformation, oxidation) to the Si framework are predicted to induce indirect-to-direct bandgap transitions.[144–146] Indeed, our computational results indicated that oxidation of the silicon framework led to structural changes, as well as an indirect-to-direct bandgap transition, depending on the degree of oxidation.[96] In regards to surface chemistry, non-terminated SiNSs (*i.e.*, silicene) are predicted to be either metallic (zero gap) or nearly metallic (small gap).[147,148] Our results demonstrated that upon fully terminating the surface with hydrogen (*i.e.*, silicane), the bandgap opens to >2.0 eV but the material is still predicted to possess an indirect bandgap with very similar Γ (2.26 eV to 2.10 eV) and M (2.16 eV to 2.05 eV) point energies,[9,96,97] consistent with computational conclusions made by others.[147,149] Further, modifying the SiNS surface to terminations other than hydrogen is predicted to have a variable impact. For instance, our computational results on fully chlorine-terminated SiNSs (Cl-SiNSs) predict that the SiNSs are still an indirect bandgap material with E_g of 1.17 eV,[97] contrary to multiple works predicting Cl-SiNSs to be a direct bandgap material with E_g of 1.70 to 2.13 eV;[149,150] however, our work predicted direct bandgaps for SiNSs with 20 or 50% chlorine termination, as well as the experimentally observed surface termination of $SiH_{0.7}Cl_{0.2}$-$(OH)_{0.1}$.[97] Similarly, full termination with thiol, hydroxyl, alkoxy, amino, cyano, or lithium groups is predicted to yield direct bandgap materials.[149]

Experimentally, the bandgap energy (E_g) of (mostly) hydrogen-terminated SiNSs has been reported to range from 2.79 to 2.20 eV with peak PL observed between approximately 440 and 560 nm,[151–154] and Φ_{PL} values of 9 to 10%;[152,155] our results are consistent with the above ranges, with peak PL mainly centered around 2.48 eV (500 nm)—although we have observed a range of 2.53 to 2.33 eV (490 to 530 nm)—and Φ_{PL} values of approximately 9% (Fig. 8(a); lower panel).[9,111,121] Our steady-state PL results, in combination with time-resolved PL suggest direct-like bandgap behaviour, consistent with our DFT predictions for H-SiNSs,[9,96,97] with our SiNSs exhibiting short carrier lifetimes (Fig. 8(b)).[111] Additionally, our PL results (Fig. 8(a); lower panel) display narrower full-width at half-maxima than other nano-Si forms like nanocrystals or porous Si.[9,96,97,111] Our results also demonstrated that the macroscopic properties of phase-pure $CaSi_2$ and resultant SiNSs have minimal to no impact on the observed optical properties (Fig. 8).[111]

As our freshly prepared SiNSs typically present with some degree of oxidation,[9,96] in the form of siloxanes,[121] and our previous band structure simulations predicted that oxidized SiNSs are direct bandgap semiconductors,[96] one potential origin of the previously observed PL is oxidation of the Si framework. Indeed, our recent study demonstrated that

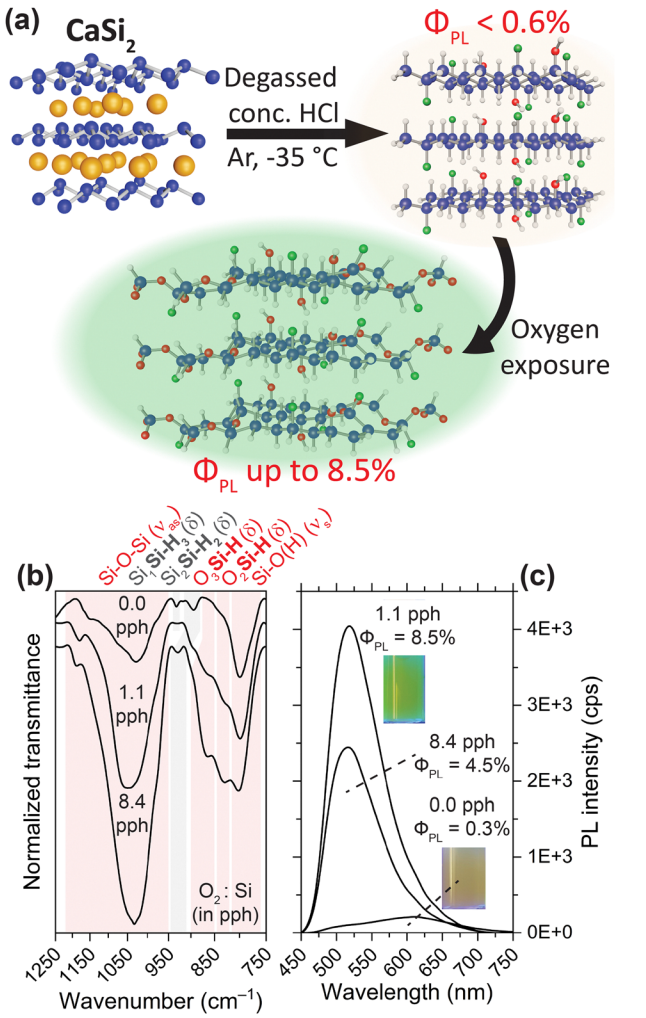

Fig. 9 (a) Schematic highlighting impacts of deintercalation of $CaSi_2$ with degassed HCl at −35 °C and subsequent oxidation of the silicon framework with dried air. (b) FTIR of SiNSs exposed to 0.0, 1.1, or 8.4 pph O_2 (relative to Si). (c) Steady-state PL spectra and associated absolute Φ_{PL} values for SiNSs exposed to 0.0, 1.1, or 8.4 pph O_2 (relative to Si). (Modified with permissions from ref. 121 Copyright 2025 Royal Society of Chemistry).

employing rigorously degassed HCl as the deintercalant yields essentially non-oxidized SiNSs (Fig. 9) with the lowest siloxane (Si–O–Si) content observed to date (without a post-deintercalation HF treatment).[121] Our SiNSs prepared through this approach were effectively non-emissive, with peak PL centered near 610 nm and Φ_{PL} values an order of magnitude lower than previously reported values for SiNSs synthesized in air-saturated HCl (<0.6% *vs.* 9%). Additionally, we attributed the weak shoulder observed near 2.43 eV (510 nm) to slight oxidation (indicated by FTIR). Indeed, when we intentionally exposed the SiNSs to incrementally larger quantities of dried air (*i.e.*, molecular oxygen), we observed increasing oxidation of the SiNSs (confirmed by FTIR; Fig. 9(b)) that was accompanied by a marked increase in the 510 nm feature and Φ_{PL} to over 8%, consistent with our DFT predictions on oxidized SiNSs,[96] after which the PL blueshifted slightly to 500 nm and the Φ_{PL} decreased below 5% (Fig. 9(c)), which we attributed to increasing SiO_2 character. We hypothesize that changes in observed PL originate from conformational alterations to the Si framework, due to oxygen insertion that further buckled the Si framework;[96,121] such conformational changes (armchair *vs.* boat-like configuration) are predicted to shift the band structure from quasi-direct to direct.[144–146] These predicted and observed electronic restructurings may arise from the laterally strained Si framework,[156] as Kim *et al.* predicted that increasing biaxial strain induces an indirect-to-direct bandgap transition.[157] We note that HF treating the SiNSs to remove these oxides has been reported to blueshift and decrease the PL, relative to the as-prepared sample.[158]

Contrary to our results on intentional SiNS oxidation,[121] our previous study, in which SiNSs were annealed at temperatures up to 450 °C, suggests that increasing SiNS oxidation (Fig. 7(c)) decreases PL (Fig. 7(d)).[96] Specifically, for annealing temperatures up to 200 °C, we observed that the relative PL intensity only decreased marginally, while increasing the annealing temperature to 300 °C reduced the PL intensity by over half the original value and higher annealing temperatures (375 °C) leading to an effectively non-photoluminescent material (Fig. 7(d)). A key difference between our two works is that annealing of the SiNSs led to homolytic cleavage of surface groups producing Si dangling bonds (evidenced by EPR; see Fig. 7(e)) and a coalesced amorphous silicon structure that decreased the PL; the former is consistent with our own DFT predictions that Si radicals (silyl groups) introduce midgap states.[96]

In addition to structural changes to the Si framework impacting the electronic properties, our results demonstrate that modulating the SiNS surface chemistry leads to noteworthy changes to the band structure and bandgap.[9,96,97] As previously mentioned, we predicted that SiNSs with a composition of $(SiH_{0.7}Cl_{0.2}(OH)_{0.1})$ are a direct bandgap material with an E_g of 1.68 eV, compared to the quasi-direct H-SiNSs with direct and indirect transitions of 2.1 and 2.05 eV, respectively.[97] More recently, we demonstrated that SiNSs with a nominally equivalent surface composition possess an experimentally observed bandgap of approximately 2.03 eV with a Φ_{PL} < 0.6% while oxidized SiNSs displayed a bandgap of approximately 2.43 eV with a Φ_{PL} > 8%.[121] Additionally, our works also demonstrated that both oxidation and annealing of the SiNSs led to the loss of these surface groups *via* currently unknown oxidative mechanisms and homolytic bond cleavage, respectively;[96,121] however, other than silyl formation upon annealing, we have yet to establish correlations between the lost surface termination and optical properties. Additionally, while we have computationally predicted the effects of chlorine (and loosely hydroxyl) termination on electronic properties,[97] we (and others) have yet to experimentally explore the impacts that increased chlorine or hydroxyl content have; however, literature suggests that the hydroxyl content of the SiNS surface can be increased *via* water exposure.[135] Lastly, we note that conflicting conclusions exist in the literature on other surface terminations (*e.g.*, alkyl), with some reporting that formation of Si–C bonds has minimal impact on the observed PL,[159] while others report both blue- and redshifts in the observed optical properties for the formation of Si–C/Si–N or Si–C bonds, respectively;[106,141,142,160] our results on SiNS oxidation[121] suggest that the observed blueshifts in these works may arise from oxidation of the silicon framework, as FTIR in these works indicated that oxidation of the Si framework occurred upon the ligand exchange from hydrogen to alkyl groups.

Similar to SiNCs, alloying the SiNSs with Ge is a promising approach for modulating the material's electronic properties. While our group has yet to contribute to this area, we want to highlight key works and conclusions for these $Si_{1-x}Ge_x$ alloyed NSs. Layered Zintl phase $CaSi_{2-2x}Ge_{2x}$ (x = 0.1–0.9) has been successfully prepared and decalciated to yield $Si_{1-x}Ge_x$ alloyed NSs using similar approaches to SiNSs.[14,110,161] Decalciation of the $CaSi_{2-2x}Ge_{2x}$ Zintl phase precursors with cold HCl is reported to yield fully hydrogen-terminated Ge sites while Si atoms are fully hydroxyl terminated, except for $Si_{1-x}Ge_x$ with $x \geq 0.5$, where the silicon sites have mixed hydrogen and hydroxyl termination.[14] Similar to SiNSs, the predicted energetically stable configuration for the deintercalated, alloyed monolayers is a buckled, armchair conformation,[15] with experimental evidence suggesting this conformation is maintained for the $Si_{1-x}Ge_x$ alloys upon deintercalation.[14,110] Termination of the $Si_{1-x}Ge_x$ alloyed NSs' surface (*e.g.*, hydrogen, hydroxyl) is predicted to open the bandgap, resulting in direct bandgap materials with E_g spanning the visible (2.45 eV) to near-infrared (1.53 eV) due to increasing Ge content redshifting the predicted bandgap.[14,15] Consistent with predictions, increasing Ge content in the $Si_{1-x}Ge_x$ alloyed NSs is reported to lead to tuneable bandgaps from the visible (2.57 eV) to the near infrared (1.53 eV);[14,110] however, to the best of our knowledge, room-temperature PL has yet to be observed. Further, these materials typically present with some degree of framework oxidation,[14,110] typically in the form of Si–O–Si (not Ge–O–Ge), which may play a role in the observed electronic properties, similar to our results for SiNSs.[121]

3.2 Germanium nanosheets

3.2.1 Synthesis. Similar to SiNSs, germanium nanosheets (GeNSs) are typically prepared from the Zintl phase calcium

digermanide ($CaGe_2$), with numerous deintercalating agents reported.[113,162–170] Two of the most commonly employed approaches involve HCl at low temperature or alkylhalides at room temperature as the deintercalating agent.[102,154,163–165,171–178] We prepared phase-pure $CaGe_2$ using an elemental melt approach, loosely equivalent to our EM-$CaSi_2$ preparation,[96,111] and decalciated the $CaGe_2$ precursor using methyliodide,[179,180] and a slightly modified synthetic procedure based on previous reports.[171]

3.2.2 Structure. The topotactic deintercalation of $CaGe_2$, typically with (mineral) acids, yields stacked Ge monolayers consisting of hexagonal, puckered sp^3 layers of germanium atoms,[163] analogous to the SiNS structure, with the stacking sequence of the Zintl phase precursor imparted to the GeNSs.[172] Given this, similar to SiNSs, understanding $CaGe_2$ polytypism is crucial,[129,172,181] since the stacking sequence can influence the electronic properties.[172] Contrary to the disorder that we observed in layered SiNSs,[96] McComb and coworkers identified turbostratic disorder in GeNSs, mainly in the form of rotational disorder, as the primary origin of the previously observed inherent *c*-axis disorder in GeNSs.[164] Further, contrary to the robust thermal stability that we observed for SiNSs,[96] amorphization of the Ge framework was demonstrated to occur at substantially lower temperatures with coalescence starting around 75 °C and complete amorphization by 175 °C,[163,173] regardless of minor surface termination other than hydrogen (–Cl, –Br, –I; *vida infra*),[163] except for alkyl termination which improves the thermal stability of the Ge framework, increasing the amorphization onset to 250 °C.[175]

3.2.3 Surface chemistry. Akin to SiNSs, deintercalation of $CaGe_2$ with acids results in hydrogen-terminated Ge monolayers.[102,154,162–165,168,173] Contrary to SiNSs though, these approaches result in GeNSs with effectively 100% hydrogen terminaton (germanane or H-GeNSs), since any formed oxides are etched by the various acids. While the reported thermal stability of the Ge framework is poor (*vide supra*), the dehydrogenation of these surface hydrogen groups was reported to occur at higher temperatures (200 to 250 °C).[173] Additionally, H-GeNSs have been reported to be remarkably stable against oxidation,[173] contrary to our results on mostly hydrogen-terminated SiNSs.[121] Similar to our results for SiNSs though,[97] terminal chlorine groups have also been reported for GeNSs, albeit at a markedly smaller ratio (1 : 50 for GeNSs *vs.* 1 : 6 for SiNSs).[97,173] Similarly, literature suggests that minor halide termination can result when deintercalating with other halide-containing chemicals (*e.g.*, HBr, HI, ICl).[163,167] Furthermore, radical- or thermal-induced hydrogermylation or Grignard strategies can be employed to modify the surface of hydrogen-terminated GeNSs to alkyl (*e.g.*, dodecane) termination.[95,167,182] In addition to these conventional approaches, other surface termination strategies have more recently been explored to yield Ge–C or Ge–S linkages.[162,183,184]

We prepared methyl-terminated GeNSs using a one-step metathesis approach in which $CaGe_2$ was simultaneously deintercalated and alkylated by methyliodide;[179,180] this approach was developed by the Goldberger group,[171,175] with multiple alkylhalides reported since, leading to numerous types of alkyl-terminated GeNSs.[170,172,174,176–178] In this approach, smaller terminal groups generally lead to near 100% surface coverage while larger, sterically bulky groups result in mixed termination, typically consisting of the alkyl group and hydrogen.[185] Given this, we chose to deintercalate $CaGe_2$ with the shortest reported alkylhalide, methyliodide.[179,180] To avoid oxidation of the GeNSs, which necessitates an HCl wash to remove the oxides, with a byproduct being chlorine termination that leads to further oxidation,[175] we conducted the deintercalation of $CaGe_2$ using a 1 : 30 : 10 : 60 molar ratio of $CaGe_2$: methyliodide : water : acetonitrile,[179,180] since Goldberger and coworkers reported that distilled acetonitrile with at least six equivalents of water is necessary for increased methyl coverage and improved air stability.[171] We observed improved thermal stability of the methyl-terminated (CH_3-) GeNSs over H-GeNSs,[180] consistent with reports that the surface demethylates between 250 and 300 °C,[175] compared to 200 to 250 °C for H-GeNSs.[173]

3.2.4 Structure–property relationships. Similar to SiNSs, when GeNSs lack any surface termination (*i.e.*, germanene), the material is predicted to be metallic.[99] Fully terminating the surface with hydrogen (*i.e.*, germanane) is predicted to result in a direct bandgap material with electronically decoupled layers[173] and E_g ranging from 1.0 to 2.3 eV.[99,186–189] Additionally, the conformation[190–192] and dimensionality[193] of H-GeNSs, as well as terminations other than hydrogen, are also predicted to modulate the materials' electronic properties.[186,187,194]

We observed that replacing hydrogen termination on GeNSs with alkyl (*i.e.*, methyl) groups, *via* deintercalation with methyliodide instead of HCl, increased the bandgap of the CH_3-GeNSs to 1.80 eV to 1.95 eV,[179,180] compared to reported values of approximately 1.3 eV to 1.6 eV for H-GeNSs,[154,162,168,173] a blueshift that is consistent with others' conclusions;[175,176,178] however, others have reported that H-GeNSs exhibit intense PL centered at approximately 1.35 eV (or 918 nm).[154,189] Additionally, we concluded that the PL of CH_3-GeNSs consists of two contributions—one from the band edge and the other from trap states—with our time-resolved measurements suggesting that the rate of trap-assisted recombination is slower than band-to-band recombination (Fig. 10).[179] Conversely, Goldberger and coworkers demonstrated that the intense PL observed at 1.87 eV for CH_3-GeNSs arises from local distortions of the Ge framework due to intercalated water,[195] with the water-induced PL comprised of two distinct exciton populations localized at recombination centers within the intercalated water;[196] thus, our previously observed PL results may originate from intercalated water. Further, the band-edge fluorescence is reported to be essentially independent of layer thickness with Φ_{PL} = 0.2%.[175] In addition to methyl termination, others have reported various effects on the observed PL for different alkyl termination, both from alkylhalide deintercalation or post-deintercalation modification,[162,174,177,178,197] with ligand-bandgap trends remaining elusive. Although, Jiang *et al.* demonstrated that installing larger, more electronegative ligands on GeNSs (*e.g.*, $-CH_3$ *vs.* $-CH_2OCH_3$) reduced E_g from 1.66 eV to 1.45 eV due to the electron-withdrawing and steric bulk of the terminal groups expanding the Ge framework.[185]

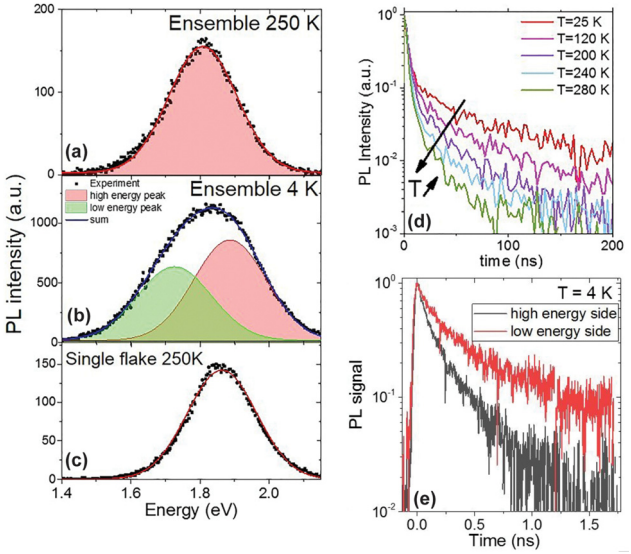

Fig. 10 PL spectra of methyl-terminated germanane flakes (a) at 250 K ensemble, (b) at 4 K ensemble, and (c) at 250 K single flake. (d) Time-resolved PL of a CH_3-GeNS film at various temperatures. (e) Time-resolved PL for a single flake of germanane at 4 K. (Modified with permission from ref. 179 Copyright 2019 AIP Publishing).

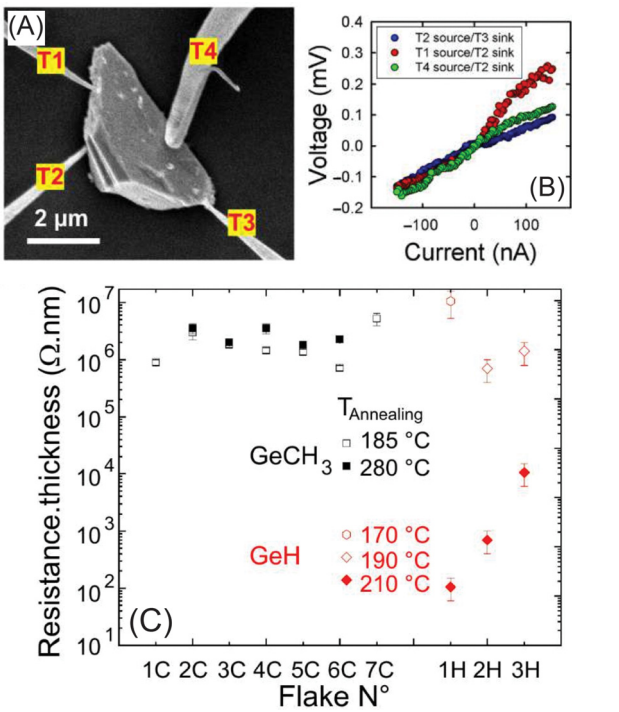

Fig. 11 (a) SEM image of a methyl-terminated germanane microcrystallite contacted with STM tips from different facets and (b) corresponding four-point resistances as a function of the position of the source tip and the grounded tip. (c) Comparison of the product of the four-point resistances to the crystallite thickness for $GeCH_3$ (C) microcrystallites and H-passivated (H) flakes, measured as a function of the annealing temperature. The spacing between the electrodes or the tips varies in a range extending from 0.5 to 3.0 µm. (Modified from ref. 180 Copyright 2022 The authors. Published by MDPI under a Creative Commons CC BY 4.0 license). http://creativecommons.org/licenses/by/4.0/, Accessed 5/15/2025.

Further, we also demonstrated that our CH_3-GeNSs display ohmic behavior that is stable at higher temperatures (280 *vs.* 190 °C) compared to H-SiNSs (Fig. 11).[180]

Lastly, akin to GeNCs, alloying the GeNSs with Sn is a promising approach to further modulate the material's electronic properties. Again, while our group has yet to contribute to this area, we want to highlight key works and conclusions for these $Ge_{1-x}Sn_x$ alloyed NSs. Layered Zintl phase $CaGe_{2-2x}Sn_{2x}$ (x = 0 to 0.25) has been successfully prepared[198,199] and decalciated to yield $Ge_{1-x}Sn_x$ alloyed NSs using cold HCl, leading to fully hydrogen-terminated germanium sites and fully hydroxyl-terminated Sn sites.[199] Similar to the other Group IV NSs, the predicted, energetically stable configuration for the deintercalated $Ge_{1-x}Sn_x$ alloyed NSs is a buckled, armchair conformation,[17] with experimental evidence suggesting this conformation is indeed maintained for $Ge_{1-x}Sn_x$ (max. of 9% Sn) alloys upon deintercalation.[199] The experimentally observed surface terminations (*e.g.*, hydrogen, hydroxyl) of the $Ge_{1-x}Sn_x$ alloys are predicted to result in direct bandgap materials with E_g spanning the near-infrared (1.72 eV) to infrared (0.68 eV), with increasing Sn content redshifting the predicted bandgap.[17] Consistent with predictions, increasing Sn content (up to 9% Sn) is reported to lead to tuneable bandgaps across the near-infrared (1.59 eV to 1.38 eV).[199] Similar to the $Si_{1-x}Ge_x$ alloyed NSs, room-temperature PL has yet to be reported for $Ge_{1-x}Sn_x$ alloyed NSs and the alloy framework is also easily oxidized (in the form of Sn–O–Sn, not Ge–O–Ge); however exposing intentionally oxidized $Ge_{1-x}Sn_x$ NSs to aq. HCl etched the oxides and restored the originally observed bandgap.[199]

4 Conclusions and outlooks

Group IV semiconductor nanomaterials are promising candidates for low-cost, fully integrated photonic and optoelectronic devices. While substantial progress has been made in understanding structure–property relationships in SiNCs, the knowledge base for other nanoscale Group IV semiconductors remains limited, largely due to the field's relative infancy compared to SiNC research. One of the most significant challenges hindering commercial application is a comprehensive understanding of the origins of PL in these materials—whether it arises from quantum confinement, surface chemistry, crystallinity/defects, or a combination. Without this understanding, controlling and optimizing the light emission remains difficult.

Elucidating the origin of light emission requires comprehensive understanding of the impact that surface chemistry has on these materials. Since the resulting surface chemistry is often highly dependent on the synthetic conditions employed, further study and refinement of various synthetic strategies are necessary to standardize the materials preparation prior to and towards photonic and optoelectronic application. Towards this, focus should be placed on correlating the relationships between synthesis/processing and surface chemistry to arrive at strategies that lead to improved control. Further, while myriad works have studied the surface chemistry of these materials, there is a substantial gap in understanding regarding how surface chemistry relates to optical properties. Thus, future work should focus on the synthesis–structure–property

relationships to arrive at improved understanding of these materials.

It is also critically important to address the stability of these materials, including (photo)chemical, electronic, thermal, and environmental stabilities. The nanoscale Group IV semiconductors often undergo structural and chemical changes (and even degradation) in the presence of oxygen and water, and these changes frequently impact their optical properties. Recently, we demonstrated that the previously observed light emission from SiNSs originates, in part, from oxidation of the silicon framework,[121] arising from poor chemical stability. Rational surface termination strategies offer a potential solution to enhance (chemical) stability, yet an in-depth understanding of how surface chemistry affects key properties, such as light emission, is still lacking. We strongly encourage the use of meticulous air-free protocols and degassed solvents,[121] especially when surface chemistry is modulated, as oxygen will oxidize the Group IV framework,[121] making deconvolution of electronic contributions challenging. Although, our recent results for SiNSs suggest that controlled oxidation could be employed as a viable route for band structure engineering.[121] Further, while altering the surface chemistry may impart a degree of chemical stability, against oxidation for instance, it may not translate to thermal stability, as organic moieties on SiNSs were reported to detach at lower temperatures[200] relative to the stability that we reported for terminations (*e.g.*, –H, –Cl, –OH) on as-prepared SiNSs (165 °C *vs.* >200 °C).[96] As robust thermal stability may be necessary for device application, thorough understanding of stability after functionalization needs established.

In summary, for the field to advance meaningfully, we believe that future research should prioritize rigorous investigation into structure–property relationships in Group IV semiconductor nanomaterials. Emphasis should be placed on unraveling the mechanisms that underlie light emission, as well as improving stability. In the case of nanoscale silicon and germanium semiconductors that are known to exhibit room-temperature light emission, the focus should shift toward refining our understanding of their structure–property dynamics and enhancing their optoelectronic performance. For alloyed Group IV semiconductor nanomaterials (*i.e.*, those containing a mixture of Si, Ge, and/or Sn), emphasis should be placed on improving stability and obtaining strong light emission that is consistent with quantum confinement. To deepen understanding, computational studies should accompany experimental work; computational models and simulations can provide valuable insight into the underlying mechanisms and offer guidance for designing materials with improved properties. With continued computational and experimental refinement of structure and surface chemistry to yield deeper insight into light-emission mechanisms, Group IV semiconductor nanomaterials may challenge III–V semiconductors for many optoelectronic applications.

Author contributions

Jeremy B. Essner: conceptualization, investigation, visualization, writing – original draft, review, and editing; Maharram Jabrayilov: investigation, visualization, writing – original draft, review, and editing; Andrew D. Tan: investigation, visualization, writing – original draft, review, and editing; Abhishek S. Chaudhari: investigation, writing – original draft; Abhijit Bera: investigation, writing – original draft; Brodrick J. Sevart: investigation, writing – original draft; Matthew G. Panthani: conceptualization, funding acquisition, resources, supervision, visualization, writing – review and editing.

Data availability

No primary research results, software or code have been included as no new data were generated or analysed as part of this feature article.

Conflicts of interest

There are no conflicts to declare.

Acknowledgements

The authors acknowledge funding from the National Science Foundation (U.S.) under awards DMR-1847370 and DMR-2350483, as well as funding from the Air Force Office of Scientific Research under Award FA9550-20-10018, all of which supported the authors and recent works from the Panthani Group cited herein. The authors also acknowledge Ryo Mizuta Graphics for providing the Blender asset for generation of nanocrystal graphics.

References

1 S. Jiang, M. Q. Arguilla, N. D. Cultrara and J. E. Goldberger, *Acc. Chem. Res.*, 2015, **48**, 144–151.
2 J. Essner and G. Baker, *Environ. Sci.: Nano*, 2017, **4**, 1216–1263.
3 J. B. Essner, D. J. Boogaart, S. N. Baker and G. A. Baker, *J. Mater. Chem. C*, 2022, **10**, 8824–8833.
4 K.-I. Saitow, *Bull. Chem. Soc. Jpn.*, 2024, **97**, uoad002.
5 R. Soref, D. Buca and S.-Q. Yu, *Opt. Photonics News*, 2016, **27**, 32–39.
6 S. Shekhar, W. Bogaerts, L. Chrostowski, J. E. Bowers, M. Hochberg, R. Soref and B. J. Shastri, *Nat. Commun.*, 2024, **15**, 751.
7 E. Oliphant, V. Mantena, M. Brod, G. J. Snyder and W. Sun, *Mater. Horiz.*, 2025, **12**, 3073–3083.
8 L. Canham, *Faraday Discuss.*, 2020, **222**, 10–81.
9 B. J. Ryan, M. P. Hanrahan, Y. Wang, U. Ramesh, C. K. A. Nyamekye, R. D. Nelson, Z. Liu, C. Huang, B. Whitehead, J. Wang, L. T. Roling, E. A. Smith, A. J. Rossini and M. G. Panthani, *Chem. Mater.*, 2020, **32**, 795–804.
10 F. Sangghaleh, I. Sychugov, Z. Yang, J. G. C. Veinot and J. Linnros, *ACS Nano*, 2015, **9**, 7097–7104.
11 H. Ueda and K.-i Saitow, *ACS Appl. Mater. Interfaces*, 2023, **16**, 985–997.
12 K. Gawarecki, J. Ziembicki, P. Scharoch and R. Kudrawiec, *J. Appl. Phys.*, 2024, **135**, 214303.
13 O. Cojocaru, A.-M. Lepadatu, G. A. Nemnes, T. Stoica and M. L. Ciurea, *Sci. Rep.*, 2021, **11**, 13582.
14 F. Zhao, Y. Feng, Y. Wang, X. Zhang, X. Liang, Z. Li, F. Zhang, T. Wang, J. Gong and W. Feng, *Nat. Commun.*, 2020, **11**, 1443.
15 P. Jamdagni, A. Kumar, A. Thakur, R. Pandey and P. K. Ahluwalia, *Mater. Res. Express*, 2015, **2**, 016301.
16 W. X. Zhang, Y. B. Wang, P. Zhao and C. He, *Phys. Chem. Chem. Phys.*, 2016, **18**, 26205–26212.

17 W. Huang, H. Yang, B. Cheng and C. Xue, *Phys. Chem. Chem. Phys.*, 2018, **20**, 23344–23351.
18 L. Taouil, A. Al-Shami and H. Ez-Zahraouy, *Mater. Sci. Semicond. Process.*, 2023, **153**, 107068.
19 M. Virgilio and G. Grosso, *J. Phys.: Condens. Matter*, 2006, **18**, 1021–1031.
20 N. Li, R. Guo, W. Chen, V. Körstgens, J. E. Heger, S. Liang, C. J. Brett, M. A. Hossain, J. Zheng and P. S. Deimel, *Adv. Funct. Mater.*, 2021, **31**, 2102105.
21 S. Shi, A. Zaslavsky and D. Pacifici, *Appl. Phys. Lett.*, 2020, **117**, 251105.
22 A. G. Cullis and L. T. Canham, *Nature*, 1991, **353**, 335–338.
23 J. D. Holmes, K. J. Ziegler, R. C. Doty, L. E. Pell, K. P. Johnston and B. A. Korgel, *J. Am. Chem. Soc.*, 2001, **123**, 3743–3748.
24 Z. Ding, B. M. Quinn, S. K. Haram, L. E. Pell, B. A. Korgel and A. J. Bard, *Science*, 2002, **296**, 1293–1297.
25 C. M. Hessel, D. Reid, M. G. Panthani, M. R. Rasch, B. W. Goodfellow, J. Wei, H. Fujii, V. Akhavan and B. A. Korgel, *Chem. Mater.*, 2011, **24**, 393–401.
26 M. G. Panthani, C. M. Hessel, D. Reid, G. Casillas, M. José-Yacamán and B. A. Korgel, *J. Phys. Chem. C*, 2012, **116**, 22463–22468.
27 Y. Yu, C. M. Hessel, T. D. Bogart, M. G. Panthani, M. R. Rasch and B. A. Korgel, *Langmuir*, 2013, **29**, 1533–1540.
28 C. M. Hessel, E. J. Henderson and J. G. C. Veinot, *Chem. Mater.*, 2006, **18**, 6139–6146.
29 M. S. Ferris, A. P. Chesney, B. J. Ryan, U. Ramesh, M. G. Panthani and K. J. Cash, *Sens. Actuators, B*, 2021, **331**, 129350.
30 W. Sun, C. Qian, X. S. Cui, L. Wang, M. Wei, G. Casillas, A. S. Helmy and G. A. Ozin, *Nanoscale*, 2016, **8**, 3678–3684.
31 S. Terada, Y. Xin and K.-I. Saitow, *Chem. Mater.*, 2020, **32**, 8382–8392.
32 J. R. R. Núñez, J. A. Kelly, E. J. Henderson and J. G. C. Veinot, *Chem. Mater.*, 2012, **24**, 346–352.
33 B. J. Stacy, L. Ngo, K. Nagasaki and B. A. Korgel, *J. Vac. Sci. Technol., A*, 2025, **43**, 013105.
34 A. N. Thiessen, M. Ha, R. W. Hooper, H. Yu, A. O. Oliynyk, J. G. C. Veinot and V. K. Michaelis, *Chem. Mater.*, 2019, **31**, 678–688.
35 B. Ghosh, T. Hamaoka, Y. Nemoto, M. Takeguchi and N. Shirahata, *J. Phys. Chem. C*, 2018, **122**, 6422–6430.
36 B. Glockzin, K. O'Connor, C. Ni, C. Butler, J. G. C. Veinot and V. K. Michaelis, *ACS Nano*, 2024, **18**, 26419–26434.
37 N. Jingu, K. Sumida, T. Hayakawa, T. Ono and K.-I. Saitow, *Chem. Mater.*, 2024, **36**, 5077–5091.
38 M. P. Hanrahan, E. L. Fought, T. L. Windus, L. M. Wheeler, N. C. Anderson, N. R. Neale and A. J. Rossini, *Chem. Mater.*, 2017, **29**, 10339–10351.
39 M. L. Mastronardi, K. K. Chen, K. Liao, G. Casillas and G. A. Ozin, *J. Phys. Chem. C*, 2015, **119**, 826–834.
40 Z. Yang, G. B. D. l Reyes, L. V. Titova, I. Sychugov, M. Dasog, J. Linnros, F. A. Hegmann and J. G. C. Veinot, *ACS Photonics*, 2015, **2**, 595–605.
41 T. Helbich, A. Lyuleeva, P. Marx, L. M. Scherf, T. K. Purkait, T. F. Fässler, P. Lugli, J. G. Veinot and B. Rieger, *Adv. Funct. Mater.*, 2017, **27**, 1606764.
42 B. Ghosh, M. Takeguchi, J. Nakamura, Y. Nemoto, T. Hamaoka, S. Chandra and N. Shirahata, *Sci. Rep.*, 2016, **6**, 36951.
43 K. Dohnalova, P. Hapala, K. Kusova and I. Infante, *Chem. Mater.*, 2020, **32**, 6326–6337.
44 T. Ono, Y. Xu, T. Sakata and K.-I. Saitow, *ACS Appl. Mater. Interfaces*, 2021, **14**, 1373–1388.
45 Y. Yu, G. Fan, A. Fermi, R. Mazzaro, V. Morandi, P. Ceroni, D.-M. Smilgies and B. A. Korgel, *J. Phys. Chem. C*, 2017, **121**, 23240–23248.
46 M. L. Mastronardi, F. Maier-Flaig, D. Faulkner, E. J. Henderson, C. Kübel, U. Lemmer and G. A. Ozin, *Nano Lett.*, 2012, **12**, 337–342.
47 D. Beri, *Mater. Adv.*, 2023, **4**, 3380–3398.
48 M. A. Islam, M. H. Mobarok, R. Sinelnikov, T. K. Purkait and J. G. C. Veinot, *Langmuir*, 2017, **33**, 8766–8773.
49 Y. Xu, S. Terada, Y. Xin, H. Ueda and K.-I. Saitow, *ACS Appl. Nano Mater.*, 2022, **5**, 7787–7797.
50 D. S. Pate, G. C. Spence, L. S. Graves, I. U. Arachchige and Ü. Özgür, *J. Phys. Chem. C*, 2024, **128**, 10483–10491.
51 I. T. Cheong, L. Y. Szepesvari, C. Ni, C. Butler, K. M. O'Connor, R. Hooper, A. Meldrum and J. G. C. Veinot, *Nanoscale*, 2024, **16**, 592–603.
52 Y. He, Q. Hao, C. Zhang, Q. Wang, W. Zeng, J. Yu, X. Yang, S. Li, X. Guo and S. Lazarouk, *J. Mater. Chem. C*, 2025, **13**, 1228–1242.
53 J. Zhou, J. Huang, H. Chen, A. Samanta, J. Linnros, Z. Yang and I. Sychugov, *J. Phys. Chem. Lett.*, 2021, **12**, 8909–8916.
54 I. N. G. Özbilgin, T. Yamazaki, J. Watanabe, H. T. Sun, N. Hanagata and N. Shirahata, *Langmuir*, 2022, **38**, 5188–5196.
55 S.-B. Qiu, Y.-T. Wang, C.-C. He, X.-L. Deng and X.-B. Yang, *Phys. Lett. A*, 2020, **384**, 126597.
56 X. D. Pi and U. Kortshagen, *Nanotechnology*, 2009, **20**, 295602.
57 L. B. Ma, T. Schmidt, O. Guillois and F. Huisken, *Appl. Phys. Lett.*, 2009, **95**, 013115.
58 S. D. Barry, Z. Yang, J. A. Kelly, E. J. Henderson and J. G. C. Veinot, *Chem. Mater.*, 2011, **23**, 5096–5103.
59 T. Kanno, M. Fujii, H. Sugimoto and K. Imakita, *J. Mater. Chem. C*, 2014, **2**, 5644–5650.
60 S. J. Lee, T. W. Kim, J. H. Song and M. E. Lee, *Bull. Korean Chem. Soc.*, 2015, **36**, 2829–2832.
61 L. Wei, H. Zhang, L. Shi and Z. Yang, *Nanoscale*, 2024, **16**, 6516–6521.
62 G. C. Spence, D. S. Pate, C. Villot, R. M. Fouzie, L. S. Graves, K. U. Lao, Ü. Özgür and I. U. Arachchige, *Nanoscale*, 2025, **17**, 3306–3321.
63 P. Reiss, M. Carrière, C. Lincheneau, L. Vaure and S. Tamang, *Chem. Rev.*, 2016, **116**, 10731–10819.
64 N. Zaitseva, Z. R. Dai, C. D. Grant, J. Harper and C. Saw, *Chem. Mater.*, 2007, **19**, 5174–5178.
65 X. Lu, K. J. Ziegler, A. Ghezelbash, K. P. Johnston and B. A. Korgel, *Nano Lett.*, 2004, **4**, 969–974.
66 H. W. Chiu and S. M. Kauzlarich, *Chem. Mater.*, 2006, **18**, 1023–1028.
67 Y. Wang, U. Ramesh, C. K. A. Nyamekye, B. J. Ryan, R. D. Nelson, A. M. Alebri, U. H. Hamdeh, A. Hadi, E. A. Smith and M. G. Panthani, *Chem. Commun.*, 2019, **55**, 6102–6105.
68 W. Sun, G. Zhong, C. Kübel, F. M. Ali, C. Qian, L. Wang, M. Ebrahimi, L. M. Reyes, A. S. Helmy and G. A. Ozin, *Angew. Chem., Int. Ed.*, 2017, **56**, 6329–6334.
69 M. Javadi, D. Picard, R. Sinelnikov, M. A. Narreto, F. A. Hegmann and J. G. C. Veinot, *Langmuir*, 2017, **33**, 8757–8765.
70 M. Javadi, V. K. Michaelis and J. G. C. Veinot, *J. Phys. Chem. C*, 2018, **122**, 17518–17525.
71 D. C. Lee, J. M. Pietryga, I. Robel, D. J. Werder, R. D. Schaller and V. I. Klimov, *J. Am. Chem. Soc.*, 2009, **131**, 3436–3437.
72 D. A. Ruddy, J. C. Johnson, E. R. Smith and N. R. Neale, *ACS Nano*, 2010, **4**, 7459–7466.
73 S. Prabakar, A. Shiohara, S. Hanada, K. Fujioka, K. Yamamoto and R. D. Tilley, *Chem. Mater.*, 2010, **22**, 482–486.
74 B. Pescara, K. A. Mazzio, K. Lips and S. Raoux, *Inorg. Chem.*, 2019, **58**, 4802–4811.
75 Z. Ju, X. Qi, R. Sfadia, M. Wang, E. Tseng, E. C. Panchul, S. A. Carter and S. M. Kauzlarich, *ACS Mater. Au*, 2022, **2**, 330–342.
76 J. Noh, H. G. Kim, D. W. Houck, T. Shah, Y. Zhang, A. Brumberg, R. D. Schaller and B. A. Korgel, *J. Am. Chem. Soc.*, 2025, **147**, 1792–1802.
77 M. Lai, L. Wei, M. Lin, H. Zhang, Y. Zhou, D. Wang, L. Shi and Z. Yang, *J. Am. Chem. Soc.*, 2025, **147**, 8125–8131.
78 J. H. Warner and R. D. Tilley, *Nanotechnology*, 2006, **17**, 3745.
79 L. M. Wheeler, L. M. Levij and U. R. Kortshagen, *J. Phys. Chem. Lett.*, 2013, **4**, 3392–3396.
80 D. D. Vaughn, J. F. Bondi and R. E. Schaak, *Chem. Mater.*, 2010, **22**, 6103–6108.
81 E. Muthuswamy, J. Zhao, K. Tabatabaei, M. M. Amador, M. A. Holmes, F. E. Osterloh and S. M. Kauzlarich, *Chem. Mater.*, 2014, **26**, 2138–2146.
82 S. Niaz, O. Gülseren, S. Hussain, M. Anwar-ul Haq, M. A. Badar and M. A. Khan, *Eur. Phys. J. Plus*, 2022, **137**, 316.
83 K. Tabatabaei, A. L. Holmes, K. A. Newton, E. Muthuswamy, R. Sfadia, S. A. Carter and S. M. Kauzlarich, *Chem. Mater.*, 2019, **31**, 7510–7521.
84 D. Carolan and H. Doyle, *J. Mater. Chem. C*, 2014, **2**, 3562–3568.
85 D. Carolan and H. Doyle, *J. Nanopart. Res.*, 2014, **16**, 2721.
86 R. J. Alan Esteves, S. Hafiz, D. O. Demchenko, Ü. Özgür and I. U. Arachchige, *Chem. Commun.*, 2016, **52**, 11665–11668.
87 D. O. Demchenko, V. Tallapally, R. J. A. Esteves, S. Hafiz, T. A. Nakagawara, I. U. Arachchige and Ü. Özgür, *J. Phys. Chem. C*, 2017, **121**, 18299–18306.

88 B. W. Boote, L. Men, H. P. Andaraarachchi, U. Bhattacharjee, J. W. Petrich, J. Vela and E. A. Smith, *Chem. Mater.*, 2017, **29**, 6012–6021.
89 V. Tallapally, T. A. Nakagawara, D. O. Demchenko, Ü. Özgür and I. U. Arachchige, *Nanoscale*, 2018, **10**, 20296–20305.
90 K. Ramasamy, P. G. Kotula, N. Modine, M. T. Brumbach, J. M. Pietryga and S. A. Ivanov, *Chem. Commun.*, 2019, **55**, 2773–2776.
91 R. C. Barbieri, K. Ding, Ü. Özgür and I. U. Arachchige, *Chem. Mater.*, 2021, **33**, 6897–6908.
92 M. Beekman, S. M. Kauzlarich, L. Doherty and G. S. Nolas, *Materials*, 2019, **12**, 1139.
93 H. Nakano and T. Ikuno, *Appl. Phys. Rev.*, 2016, **3**, 040803.
94 F. Bechstedt, P. Gori and O. Pulci, *Prog. Surf. Sci.*, 2021, **96**, 100615.
95 W. L. B. Huey and J. E. Goldberger, *Chem. Soc. Rev.*, 2018, **47**, 6201–6223.
96 B. J. Ryan, L. T. Roling and M. G. Panthani, *ACS Nano*, 2021, **15**, 14557–14569.
97 R. W. Dorn, B. J. Ryan, S. N. S. Lamahewage, M. V. Dodson, J. B. Essner, R. Biswas, M. G. Panthani and A. J. Rossini, *Chem. Mater.*, 2023, **35**, 539–548.
98 W. Wei, Y. Dai, B. Huang and T. Jacob, *Phys. Chem. Chem. Phys.*, 2013, **15**, 8789–8794.
99 H. T. Nguyen-Truong, V. Van On and M.-F. Lin, *J. Phys.: Condens. Matter*, 2021, **33**, 355701.
100 F. Zaabar, F. Mahrouche, S. Mahtout, F. Rabilloud and K. Rezouali, *J. Phys.: Condens. Matter*, 2023, **35**, 175502.
101 O. D. Restrepo, R. Mishra, J. E. Goldberger and W. Windl, *J. Appl. Phys.*, 2014, **115**, 033711.
102 J. R. Young, B. Chitara, N. D. Cultrara, M. Q. Arguilla, S. Jiang, F. Fan, E. Johnston-Halperin and J. E. Goldberger, *J. Phys.: Condens. Matter*, 2016, **28**, 034001.
103 D. Karar, N. R. Bandyopadhyay, A. K. Pramanick, D. Acharyya, G. Conibeer, N. Banerjee, O. E. Kusmartseva and M. Ray, *J. Phys. Chem. C*, 2018, **122**, 18912–18921.
104 Y. Furusawa, O. Kubo, R. Yamamoto, Y. Suzuki, N. Matsuura, Y. Hiraoka, H. Tabata and M. Katayama, *Jpn. J. Appl. Phys.*, 2023, **62**, 030905.
105 X. Deng, H. Chen and Z. Yang, *J. Semicond.*, 2023, **44**, 041101.
106 H. Nakano, Y. Tanaka, K. Yamamoto, H. Kadowaki, M. Nakashima, T. Matsui, S. Shirai, M. Ohashi and J. Ohshita, *Adv. Opt. Mater.*, 2019, **7**, 1900696.
107 N. Liu, H. Qiao, K. Xu, Y. Xi, L. Ren, N. Cheng, D. Cui, X. Qi, X. Xu, W. Hao, S. X. Dou, Y. Du, N. Liu, L. Ren, N. Cheng, X. Xu, S. X. Dou, Y. Du, H. Qiao, X. Qi, K. Xu, Y. Xi, D. Cui and W. Hao, *Small*, 2020, **16**, 2000283.
108 C. Li, J. Kang, J. Xie, Y. Wang, L. Zhou, H. Hu, X. Li, J. He, B. Wang and H. Zhang, *J. Mater. Chem. C*, 2020, **8**, 16318–16325.
109 R. Gonzalez-Rodriguez, R. M. Del Castillo, E. Hathaway, Y. Lin, J. L. Coffer and J. Cui, *ACS Appl. Nano Mater.*, 2022, **5**, 4325–4335.
110 P. K. Roy, T. Hartman, J. Šturala, J. Luxa, M. Melle-Franco and Z. Sofer, *ACS Appl. Mater. Interfaces*, 2023, **15**, 25693–25703.
111 B. J. Ryan, G. Bhaskar, J. B. Essner, A. Bera, R. W. Dorn, Y. Guo, Q. Hua Wang, A. J. Rossini, J. V. Zaikina, L. T. Roling and M. G. Panthani, *ACS Appl. Nano Mater.*, 2023, **6**, 10054–10063.
112 H. Lin, W. Qiu, J. Liu, L. Yu, S. Gao, H. Yao, Y. Chen and J. Shi, *Adv. Mater.*, 2019, **31**, 1903013.
113 Y. Georgantas, T. Giousis, F. P. Moissinac, G. R. Tainton, S. J. Haigh and M. A. Bissett, *Small Methods*, 2024, **9**, 2400964.
114 X. Lv, N. Li, Y. Li, Q. Ma, Z. Xie and S. Zhou, *Molecules*, 2023, **28**, 2143.
115 Y. Lei, D. Yang and D. Li, *Materials*, 2023, **16**, 1079.
116 C. Jia, F. Zhang, N. Zhang, Q. Li, X. He, J. Sun, R. Jiang, Z. Lei and Z. H. Liu, *ACS Nano*, 2023, **17**, 1713–1722.
117 H. Li, Y. Wang, X. Dai, Y. Gao, G. Lu, Z. Fang, H. He, J. Huang and Z. Ye, *J. Mater. Chem. C*, 2021, **9**, 10065–10072.
118 M. Stavrou, A. Stathis, I. Papadakis, A. Lyuleeva-Husemann, E. Koudoumas and S. Couris, *Nanomaterials*, 2022, **12**, 90.
119 M. Stavrou, A. M. Mühlbach, V. Arapakis, E. Groß, T. Kratky, S. Günther, B. Rieger and S. Couris, *Nanoscale*, 2023, **15**, 16636–16649.
120 B. J. Ryan, B. T. Diroll, Y. Guo, C. J. Dolgos, Q. H. Wang, L. T. Roling and M. G. Panthani, *ECS Trans.*, 2021, **102**, 3.
121 J. B. Essner, A. Bera, M. Jabrayilov, A. Chaudhari, B. T. Diroll, J. V. Zaikina and M. G. Panthani, *Nanoscale Horiz.*, 2025, **10**, 605–615.
122 S. Yamanaka, H. Matsu-ura and M. Ishikawa, *Mater. Res. Bull.*, 1996, **31**, 307–316.
123 J. R. Dahn, B. M. Way, E. Fuller and J. S. Tse, *Phys. Rev. B:Condens. Matter Mater. Phys.*, 1993, **48**, 17872–17877.
124 F. Wöhler, *Justus Liebigs Ann. Chem.*, 1863, **127**, 257–274.
125 A. Weiss, G. Beil and H. Meyer, *Z. Naturforsch., B*, 1980, **35**, 25–30.
126 H. Kautsky and G. Herzberg, *Z. Anorg. Allg. Chem.*, 1924, **139**, 135–160.
127 E. Hengge, *Top. Curr. Chem.*, 1974, **51**, 95.
128 V. H. Kautsky, W. Vogell and F. Oeters, *Z. Naturforsch., B*, 1955, **10**, 597–598.
129 R. Yaokawa, A. Nagoya and H. Nakano, *J. Solid State Chem.*, 2021, **295**, 121919.
130 X.-J. Feng, W. Carrillo-Cabrera, A. Ormeci, M. Krnel, U. Burkhardt, B. Böhme, Y. Grin and M. Baitinger, *Inorg. Chem.*, 2024, **63**, 10557–10567.
131 G. Yao, E. Pradhan, Z. Yang and T. Zeng, *Nano Lett.*, 2025, **25**, 1697–1705.
132 R. Fu, K. Zhang, R. P. Zaccaria, H. Huang, Y. Xia and Z. Liu, *Nano Energy*, 2017, **39**, 546–553.
133 X. Deng, X. Zheng, T. Yuan, W. Sui, Y. Xie, O. Voznyy, Y. Wang and Z. Yang, *Chem. Mater.*, 2021, **33**, 9357–9365.
134 M. Li, R. Ramachandran, T. Sakthivel, F. Wang and Z. X. Xu, *Chem. Eng. J.*, 2021, **421**, 129728.
135 Y. You, Y. X. Zhu, J. Jiang, M. Wang, Z. Chen, C. Wu, J. Wang, W. Qiu, D. Xu, H. Lin and J. Shi, *J. Am. Chem. Soc.*, 2022, **144**, 14195–14206.
136 Y. Sugiyama, H. Okamoto and H. Nakano, *Chem. Lett.*, 2010, **39**, 938–939.
137 L. Wang, U. S. Schubert and S. Hoeppener, *Chem. Soc. Rev.*, 2021, **50**, 6507–6540.
138 T. Helbich, M. J. Kloberg, R. Sinelnikov, A. Lyuleeva, J. G. C. Veinot and B. Rieger, *Nanoscale*, 2017, **9**, 7739–7744.
139 A. Lyuleeva, A. Rivadeneyra, T. Helbich, P. Holzmüller, B. Rieger, P. Lugli and M. Becherer, *J. Phys.:Conf. Ser.*, 2018, **1092**, 012080.
140 H. Nakano, M. Nakano, K. Nakanishi, D. Tanaka, Y. Sugiyama, T. Ikuno, H. Okamoto and T. Ohta, *J. Am. Chem. Soc.*, 2012, **134**, 5452–5455.
141 Y. Sugiyama, H. Okamoto, T. Mitsuoka, T. Morikawa, K. Nakanishi, T. Ohta and H. Nakano, *J. Am. Chem. Soc.*, 2010, **132**, 5946–5947.
142 J. Ohshita, K. Yamamoto, D. Tanaka, M. Nakashima, Y. Kunugi, M. Ohashi and H. Nakano, *J. Phys. Chem. C*, 2016, **120**, 10991–10996.
143 A. Nayad, A. Hasnaoui, Y. Hadouch, L. Fkhar, R. Idouhli, A. Abdessalam, A. Mehdi, B. Dikici, D. Mezzane, L. E. Firdoussi and M. Ait Ali, *Silicon*, 2023, **15**, 321–335.
144 M. Houssa, E. Scalise, K. Sankaran, G. Pourtois, V. V. Afanas'Ev and A. Stesmans, *Appl. Phys. Lett.*, 2011, **98**, 223107.
145 L. C. Lew Yan Voon, E. Sandberg, R. S. Aga and A. A. Farajian, *Appl. Phys. Lett.*, 2010, **97**, 163114.
146 P. Zhang, X. D. Li, C. H. Hu, S. Q. Wu and Z. Z. Zhu, *Phys. Lett. A*, 2012, **376**, 1230–1233.
147 R. Wang, X. Pi, Z. Ni, Y. Liu and D. Yang, *RSC Adv.*, 2015, **5**, 33831–33837.
148 M. Barhoumi, K. Lazaar and M. Said, *J. Mol. Graphics Modell.*, 2019, **91**, 72–79.
149 G. Yao, E. Pradhan, Z. Yang and T. Zeng, *Phys. Chem. Chem. Phys.*, 2025, **27**, 4845–4857.
150 U. Khan, M. U. Saeed, H. O. Elansary, I. M. Moussa, A. U. R. Bacha and Y. Saeed, *RSC Adv.*, 2024, **14**, 4844–4852.
151 M. Stutzmann, M. S. Brandt, M. Rosenbauer, J. Weber and H. D. Fuchs, *Phys. Rev. B:Condens. Matter Mater. Phys.*, 1993, **47**, 4806–4809.
152 S. Mondal, T. K. Mondal, Y. K. Su and S. K. Saha, *J. Colloid Interface Sci.*, 2020, **562**, 453–460.
153 T. Helbich, A. Lyuleeva, T. Ludwig, L. M. Scherf, T. F. Fässler, P. Lugli and B. Rieger, *Adv. Funct. Mater.*, 2016, **26**, 6711–6718.
154 G. Vogg, M. S. Brandt and M. Stutzmann, *Adv. Mater.*, 2000, **12**, 1278–1281.
155 U. Dettlaff-Weglikowska, W. Hönle, A. Molassioti-Dohms, S. Finkbeiner and J. Weber, *Phys. Rev. B:Condens. Matter Mater. Phys.*, 1997, **56**, 13132–13140.
156 A. Fleurence, R. Friedlein, T. Ozaki, H. Kawai, Y. Wang and Y. Yamada-Takamura, *Phys. Rev. Lett.*, 2012, **108**, 245501.

157 B. H. Kim, M. Park, G. Kim, K. Hermansson, P. Broqvist, H. J. Choi and K. R. Lee, *J. Phys. Chem. C*, 2018, **122**, 15297–15303.
158 K. Nishimura, Y. Nagao, S. Yamanaka and H. Matsu-ura, *Jpn. J. Appl. Phys.*, 1996, **35**, L293.
159 T. Helbich, A. Lyuleeva, I. M. D. Höhlein, P. Marx, L. M. Scherf, J. Kehrle, T. F. Fässler, P. Lugli and B. Rieger, *Chem. – Eur. J.*, 2016, **22**, 6194–6198.
160 J. Ohshita, Y. Tanaka, K. Yamamoto, H. Kadowaki, M. Nakashima, Y. Adachi, M. Ohashi and H. Nakano, *J. Phys. Chem. C*, 2020, **124**, 17347–17351.
161 E. Kovalska, B. Wu, L. Liao, V. Mazanek, J. Luxa, I. Marek, L. Lajaunie and Z. Sofer, *ACS Nano*, 2023, **17**, 11374–11383.
162 T. Giousis, P. Zygouri, N. Karouta, K. Spyrou, M. Subrati, D. Moschovas, M. C. A. Stuart, H. Hemmatpour, D. P. Gournis and P. Rudolf, *Small*, 2024, **20**, 2403277.
163 S. Jiang, E. Bianco and J. E. Goldberger, *J. Mater. Chem. C*, 2014, **2**, 3185–3188.
164 A. H. Trout, Y. Wang, B. D. Esser, S. Jiang, J. E. Goldberger, W. Windl and D. W. McComb, *J. Mater. Chem. C*, 2019, **7**, 10092–10097.
165 C. Ni, K. M. O'Connor, J. Trach, C. Butler, B. Rieger and J. G. Veinot, *Nanoscale Horiz.*, 2023, **8**, 1217–1225.
166 N. Liu, G. Bo, Y. Liu, X. Xu, Y. Du and S. X. Dou, *Small*, 2019, **15**, 1805147.
167 J. Sturala, J. Luxa, S. Matějková, Z. Sofer and M. Pumera, *Nanoscale*, 2019, **11**, 19327–19333.
168 T. Giousis, G. Potsi, A. Kouloumpis, K. Spyrou, Y. Georgantas, N. Chalmpes, K. Dimos, M.-K. Antoniou, G. Papavassiliou, A. B. Bourlinos, H. J. Kim, V. K. S. Wadi, S. Alhassan, M. Ahmadi, B. J. Kooi, G. Blake, D. M. Balazs, M. A. Loi, D. Gournis and P. Rudolf, *Angew. Chem., Int. Ed.*, 2021, **60**, 360–365.
169 E. Kovalska, N. Antonatos, J. Luxa and Z. Sofer, *ACS Nano*, 2021, **15**, 16709–16718.
170 Z. Liu, Z. Wang, Q. Sun, Y. Dai and B. Huang, *Appl. Surf. Sci.*, 2019, **467**, 881–888.
171 S. Jiang, M. Q. Arguilla, N. D. Cultrara and J. E. Goldberger, *Chem. Mater.*, 2016, **28**, 4735–4740.
172 N. D. Cultrara, Y. Wang, M. Q. Arguilla, M. R. Scudder, S. Jiang, W. Windl, S. Bobev and J. E. Goldberger, *Chem. Mater.*, 2018, **30**, 1335–1343.
173 E. Bianco, S. Butler, S. Jiang, O. D. Restrepo, W. Windl and J. E. Goldberger, *ACS Nano*, 2013, **7**, 4414–4421.
174 H. Tachibana, N. Toda, N. Takada, T. Mizokuro, A. Ando and R. Azumi, *Jpn. J. Appl. Phys.*, 2019, **58**, SIIB21.
175 S. Jiang, S. Butler, E. Bianco, O. D. Restrepo, W. Windl and J. E. Goldberger, *Nat. Commun.*, 2014, **5**, 3389.
176 H. Tachibana, N. Toda, N. Takada and R. Azumi, *Jpn. J. Appl. Phys.*, 2019, **58**, 105002.
177 J. Sturala, J. Luxa, S. Matějková, J. Plutnar, T. Hartman, M. Pumera and Z. Sofer, *Chem. Mater.*, 2019, **31**, 10126–10134.
178 S. Ng, J. Sturala, J. Vyskocil, P. Lazar, J. Martincova, J. Plutnar and M. Pumera, *ACS Nano*, 2021, **15**, 11681–11693.
179 C. Livache, B. J. Ryan, U. Ramesh, V. Steinmetz, C. Gréboval, A. Chu, T. Brule, S. Ithurria, G. Prévot, T. Barisien, A. Ouerghi, M. G. Panthani and E. Lhuillier, *Appl. Phys. Lett.*, 2019, **115**, 052106.
180 D. Sciacca, M. Berthe, B. J. Ryan, N. Peric, D. Deresmes, L. Biadala, C. Boyaval, A. Addad, O. Lancry, R. Makarem, S. Legendre, D. Hocrelle, M. G. Panthani, G. Prévot, E. Lhuillier, P. Diener and B. Grandidier, *Nanomaterials*, 2022, **12**, 1128.
181 R. Yaokawa, A. Nagoya, K. Mukai and H. Nakano, *Acta Mater.*, 2018, **151**, 347–355.
182 H. Yu, T. Helbich, L. M. Scherf, J. Chen, K. Cui, T. F. Fässler, B. Rieger and J. G. C. Veinot, *Chem. Mater.*, 2018, **30**, 2274–2280.
183 T. Hartman, J. Šturala, J. Luxa and Z. Sofer, *ACS Nano*, 2020, **14**, 7319–7327.
184 Á. Campos-Lendinez, J. Faraudo, J. García-Antón, X. Sala and J. Muñoz, *ACS Appl. Mater. Interfaces*, 2024, **16**, 66280–66289.
185 S. Jiang, K. Krymowski, T. Asel, M. Q. Arguilla, N. D. Cultrara, E. Yanchenko, X. Yang, L. J. Brillson, W. Windl and J. E. Goldberger, *Chem. Mater.*, 2016, **28**(21), 8071–8077.
186 H. Jia, R. Wang, Z. Ni, Y. Liu, X. Pi and D. Yang, *J. Mater. Sci. Technol.*, 2017, **33**, 59–64.
187 I. Kupchak, F. Bechstedt, O. Pulci and P. Gori, *Sci. Rep.*, 2024, **14**, 25182.
188 Y. Ma, Y. Dai, Y. B. Lu and B. Huang, *J. Mater. Chem. C*, 2014, **2**, 1125–1130.
189 Z. Hajnal, G. Vogg, L. J.-P. Meyer, B. Szücs, M. S. Brandt and T. Frauenheim, *Phys. Rev. B:Condens. Matter Mater. Phys.*, 2001, **64**, 033311.
190 D. Kaltsas, T. Tsatsoulis, O. G. Ziogos and L. Tsetseris, *J. Chem. Phys.*, 2013, **139**, 124709.
191 H. Shu, Y. Li, S. Wang and J. Wang, *Phys. Chem. Chem. Phys.*, 2015, **17**, 4542–4550.
192 J. Rivera-Julio, A. González-Garcia, R. González-Hernández, W. López-Pérez, F. M. Peeters and A. D. Hernández-Nieves, *J. Phys.: Condens. Matter*, 2019, **31**, 075301.
193 Y. Zhou, X. Li, Z. Wang, S. Li and X. Zu, *Phys. Chem. Chem. Phys.*, 2014, **16**, 18029–18033.
194 Y. Jing, X. Zhang, D. Wu, X. Zhao and Z. Zhou, *J. Phys. Chem. Lett.*, 2015, **6**, 4252–4258.
195 T. J. Asel, W. L. B. Huey, B. Noesges, E. Molotokaite, S. C. Chien, Y. Wang, A. Barnum, C. McPherson, S. Jiang, S. Shields, C. D'Andrea, W. Windl, E. Cinquanta, L. J. Brillson and J. E. Goldberger, *Chem. Mater.*, 2020, **32**(4), 1537–1544.
196 E. Cinquanta, S. Sardar, W. L. B. Huey, C. Vozzi, J. E. Goldberger, C. D'Andrea and C. Gadermaier, *Nano Lett.*, 2022, **22**, 1183–1189.
197 J. Muñoz, M. Palacios-Corella, I. J. Gómez, L. Zajíčková and M. Pumera, *Adv. Mater.*, 2022, **34**, 2206382.
198 A. Ganguli and J. Corbett, *J. Solid State Chem.*, 1993, **107**, 480–488.
199 M. Q. Arguilla, S. Jiang, B. Chitara and J. E. Goldberger, *Chem. Mater.*, 2014, **26**, 6941–6946.
200 H. Okamoto, Y. Kumai, Y. Sugiyama, T. Mitsuoka, K. Nakanishi, T. Ohta, H. Nozaki, S. Yamaguchi, S. Shirai and H. Nakano, *J. Am. Chem. Soc.*, 2010, **132**(8), 2710–2718.